Energy Storage

WILEY

ENERGY STORAGE

RESEARCH ARTICLE

Optimization and Numerical Analysis of an Air and Phase Change Material Cooled Lithium-Ion Battery Pack

Vineet Singh[1] | Vaibhav Trivedi[2] | V. R. Mishra[1]

[1]Department of Mechanical Engineering, School of Engineering & Technology, IFTM University, Moradabad, India | [2]Department of Mechanical Engineering, G. L. Bajaj Institute of Management and Technology, Greater Noida, India

Correspondence: Vineet Singh (vineetpsh@gmail.com)

Received: 3 July 2025 | **Revised:** 18 November 2025 | **Accepted:** 15 December 2025

Keywords: air | cooling | lithium-ion cell | optimization | phase change material | response surface methodology

ABSTRACT

Increasing demand for fast charging in electric vehicles requires battery cooling. This research article explored the outcome of air cooling and phase change material (PCM) on battery thermal management at several charging rates. Initially, the numerical investigation was carried out on two different models of the air and PCM (paraffin wax, n-eicosane, and copper foam) cooling. Outcomes of the air-cooling show that air cooling is not feasible for higher charging rates, especially more than 2 C. Consequently, response surface methodology was used to determine the consequence of air inlet velocity, air inlet temperature, and charging rates on the temperature of the battery pack. The optimum conditions for air cooling are heat generation 42 102 W/m^3, air inlet velocity 0.5 m/s, and inlet air temperature 20°C, for which the responses are, namely, maximum cell temperature 332.62 K, cooling efficiency 9.73%, pressure drop 6.53 Pa, and outlet air temperature 313.92 K. The copper foam gives a lower temperature and also maintains uniformity in the maximum cell temperature as associated to other PCM. The PCM materials fail to cool all the cells uniformly due to the lesser thermal conductivity of the PCM materials. The current simulation study validated with the experimental study of previous researchers, which shows that the copper foam gives better performance than the composite PCM. At 50 min of charging, the copper foam and CPCM enhance the maximum cell temperature up to 66°C and 71°C. The copper foam performed best at the 3 C charging with 50 min, at which the maximum cell temperature was 339 K.

1 | Introduction

The current energy scenario moves toward green energy sources due to the need for environmental sustainability. The green energy source is nonpolluting in nature, and due to that, these fuels are used in various applications. In the field of transport, the evolution of electric cars is cost-effective and eco-friendly. These electric cars run by the use of lithium-ion batteries (LIBs). Additionally, LIBs have several advantages over other batteries. The high energy per unit volume, longer duration, and shorter charging period attract industries to use LIBs in automobiles [1]. Additionally, LIBs have increasing performance as compared to other power batteries [2]. LIBs in the form of a pack have several individual cells. At the time of the operation, these cells generate heat, which enhances the average temperature of the battery pack, which sometimes catches fire and harms the life of the passengers.

It has been noted from the previous research that if the temperature of the cell is enhanced to more than 40°C, significant drops in power production of the cell were noted [3]. It was also noted that if the temperature of the cell was amplified from 50°C, then the 60% power storage capacity of the cell was reduced [4]. So, to augment the life and the charging capacity of the cells, the cell temperature must be sustained inside the range of 15°C–24°C [5]. This can happen by the use of battery thermal management technique (BTMT) for LIBs. The thermal management techniques remove the trapped heat from the cell

by using cooling fluids. The air, liquid, and PCM materials are the most important fluids which are used to cool the batteries. Among all fluids, air cooling has numerous advantages like being economical, having lower weight, and being easy to implement without much modification in the design [6]. However, due to the low heat transfer coefficient, air cooling cannot cool the battery in the optimum temperature range at high heat generation. The heat transfer rate has to be augmented either by changing the flow section to create turbulence or by enhancing the mass flow rate; both cases raise the pressure in the flow path [7].

The air cooling may be a better solution of the BTMS if the cooled air is sent in place of the dry atmospheric air. It was reported that the battery is submerged in a pool of saturated liquid of the refrigerant R-134a. This system maintained the temperature of the battery well within the optimum range of 35°C [8]. Liquid fluids have better options due to their good thermal properties than air. However, liquid cooling incurs a higher cost, is corrosive in nature, and is heavier than air cooling. The cooling effect can be enhanced either through changes in the design's structure or by modifying the thermal properties of the cooling fluids. Siruvuri et al. [9] used water as a coolant for lowering the temperature of the prismatic cell. The observations of the study included the effect of heat generation and water flow rate on temperature variation. They concluded that at the water discharge of $1.6 \times 10^{-6}\,m^3/s$, the temperature drop of 5.85°C was achieved through this cooling technique. Mohsen et al. [10] analyzed a hybrid liquid water and phase change material as the coolant for a battery pack. The investigation has been conducted to maintain the LIB temperature at an optimal level under very low environmental conditions of 0°C. The results revealed that the hybrid cooling system maintained a 5.5°C higher temperature than the aluminum plate liquid-cooling system.

Kausthubharam et al. [11] examined the performance of the 20 Ah pouch cell with liquid water cooling. The liquid cooling maintained the consistency in the temperature distribution and lowered the maximum temperature to 20% less than without a water-cooled lithium-ion cell. However, the mini-channel enhances the pressure drop simultaneously. Jiang et al. [12] investigated a LIB pack considering the 18 cells with pulsating liquid water cooling, heat pipe, and airflow duct section. The outcomes of the study revealed that the mist liquid cooling with a 3 C discharge rate reduced the average battery temperature by 32. Chen et al. [13] evaluated a 40 LIB pack under pure PCM, composite PCM, and hybrid PCM fluids cooling. Investigation shows that pure PCM has lower thermal conductivity which shows the maximum temperature of the cell surface. Lu et al. [14] designed and developed the battery cooling with PCM and liquid cooling. The results indicated that in the initial 600 s, the one cell temperature climbed above 80°C which is within the range of the optimum temperature. An et al. [15] investigated battery cooling by the PCM material and liquid cooling. The paraffin wax and expanded graphite were used as composite phase change material for maintaining the battery cell temperature well within the desirable temperature at a 3 C discharging rate. The effect of the fraction of expanded graphite at various concentrations in paraffin wax and channel arrangement was investigated to know the temperature variation of the battery. Furthermore, the outcomes showed that a temperature drop of 2.1°C was obtained through this technique as compared to pure PCM at 6% weight concentration. Zhao et al. [16] evaluated the cooling effect of the copper foam/paraffin as the composite phase change material with liquid water. Additionally, the numerical results were validated with the experimental study under various Reynolds numbers. The study revealed that liquid cooling helps to enhance the temperature in cold environments and simultaneously reduces the temperature in hot environments. Rahmani et al. [17] focused on designing and simulating the BTMS with MATLAB Simulink. The investigation was carried out to know the effect of the slope of the road and driving on the performance of the electric vehicle. The outcomes of the study indicated that 10° road slope required the maximum thermal load, which enhanced the battery temperature up to 26.7°C with refrigerant consumption rising up to 45 868.28 kW at 50°C atmospheric temperature. Pusapati et al. used PCM material to cool the battery temperature in electric vehicles at various C rates.

Table 1 summarizes the various techniques and designs previously applied in battery cooling. The number of cooling fluids, such as water, PCM, nanofluids, and immersion oil, used to cool the battery pack. Liquid-cooling methods are costly and corrosive; even the system will require significant design changes to implement the technology. On the other hand, the air and PCM hybrid cooling is simple, compact, lightweight, and has a higher latent heat absorption capacity. Due to the numerous benefits of the air and PCM material, this research focused on comparing the air, paraffin wax, N-eicosane, and copper foam cooling on battery pack temperature, which is novel and not reported in earlier research. This research likewise performed the optimization with the air cooling based on the inlet air velocity, inlet air temperature, and heat generation to know the optimum air inlet temperature and velocity to cool the battery pack. This is very helpful for future study to know the optimum inlet air temperature, which can be conditioned and cooled by the refrigerant. Overall, this study provides a region of safety for a LIB pack under air and PCM material cooling.

1.1 | Research Objectives of the Study

In this analysis, a battery pack that has 24 cells of the lithium ion has been investigated under the cooling of air and PCM materials. The following are the research objectives of the study.

a. Performed the numerical simulation of air cooled 24-cell LIB pack at different charging rates.
b. For determining the best setting of the input air conditions, the optimized by RSM.
c. Similar to air, the new geometry of the battery pack cooled by PCM is prepared in the design modeler and analyzed at different charging rates, and determines the volume fractions and temperature contour of the battery.
d. Compared the temperature of the battery pack under air and PCM material cooling.
e. Finally, conclude the research investigation on battery under air and PCM material cooling at 1, 2, and 3 C charging rates.

TABLE 1 | Various cooling techniques used in previous literature for cooling battery pack.

S. no.	Authors description	Techniques used	Finding from the research
1	Hasan et al. (2025) [18]	Used SiO_2 nanoparticles in water for cooling the battery pack	• Smallest nanoparticle size gives the maximum Nusselt number. • For particle sizes 50, 40, 30, and 20 nm. The Nusselt number increased to be 2.8%, 5.5%, 11.6%, and 22.6%, respectively.
2	Li et al. (2025) [19]	Immersion water and PCM material used as cooling fluid.	• The extreme temperature and temperature difference were lowered to be 4.26% and 10.8%, respectively.
3	Joshi et al. (2025) [20]	Battery pack cooled in three different configurations, aligned, staggered, and circular.	• The staggered configuration has the lowest cell temperature of (307–316 K). • The circular structure of LIB cells has minimum pumping power, it requires 40 and 25 W lower power as compared to the staggered and aligned cell configuration.
4	Yang et al. (2024) [21]	Forced air and PCM material are both used synergistically for cooling the pack.	• The lowest temperature of the pack was obtained to be 29.71°C at 12 mm PCM material thickness. • The PCM alone was not sufficiently cool the battery pack.
5	Xin et al. (2023) [22]	A liquid passage is provided to cool the cells by liquid water, and a crossed flow forces air to pass over the cell surface.	• The liquid and air were both fluids involved in cooling, giving maximum cooling. • The maximum temperature, temperature drop and pressure drop obtained to be 36.82°C, 2.76°C, and 2.62 Pa at flow rate of 0.0012 kg/s.
6	Chakir et al. (2025) [23]	A thermoelectric cooler and serpentine heat exchanger have been used to cool the TEC plate.	• Increased the Nusselt number 101% as compared to thinner plate. • The maximum heat exchange happens at an aspect ratio of 0.2. • The heat transfer increased upto 28.15% at an aspect ratio of 0.8.
7	Tousi et al. (2024) [24]	A battery pack cooled by the use of Al_2O_3–water nano fluid.	• 4% volume fraction of Al_2O_3 at 0.3 m/s gives the maximum cooling effect. • If the flow velocity rises from 0.2 m/s to 0.3 m/s, the battery cell's maximum and nonuniformity in temperature reduced from 1.06°C to 0.26°C
8	Dilbaz et al. (2024) [25]	A pouch cell of 20 Ah cooled by PCM, water and nanofluid at various discharging rates.	• In 3, 4, and 5 C discharging, the battery cell maximum temperature reached above 50°C. • In liquid cooling, the increase in Reynolds Number reduces the lower down the maximum temperature.
9	Kumaran et al. (2024) [26]	This study investigated the immersion cooling of the 4S2P LIBs battery at 3 C discharging rate. Additionally, comparison was made between ester oil and air in natural and forced convection.	• Easter oil reduced the maximum cell temperature 3.3% as compared to air cooling in natural convection. • Easter oil with forced convection maintained the 5°C lower temperature at fluid velocity 0.077 m/s as compared to forced air convection.
10	Cheng et al. (2024) [27]	Designed and developed a compact container in which cells were dipped for marinating the temperature of the cell an optimum level.	• Study revealed that the maximum temperature in silicon oil, white oil and transformer oil was 53°C, 47.3°C, and 45.6°C, respectively at the 2 C discharging conditions. • The maximum temperature reduced by 25%, 33%, and 35% as associated to natural convection cooling in which the extreme temperature reached 70.5°C. • The results indicated that the transformer oil proved to excellent cooling effect as compared to other oils.

2 | Thermal Modeling of the Lithium Ion Cells

2.1 | Cell Surface Temperature

Figure 1 represents the top view of the single-cell LIB cell. The generated heat inside the cell is conducted by the surrounding air.

$$q \times \pi R^2 L = h \times 2\pi RL \times \left(T_S - T_{\text{atm}}\right) \tag{1}$$

$$T_S = T_{\text{atm}} + \frac{qR}{2h} \tag{2}$$

2.2 | Temperature Variation Within the Cell

Apply the heat conduction equation inside the cylindrical shell at steady state

$$-\frac{kA_r dT}{dr} = q \times V_r \tag{3}$$

$$-K \times \frac{2\pi RLdT}{dr} = q \times \pi R^2 L \tag{4}$$

$$dT = -\frac{q}{2k} r dr \tag{5}$$

Integrate the equation

$$T = -\frac{q}{4k} r^2 + C_1 \tag{6}$$

Apply the boundary condition at $r = R$, $T = T_S$

$$T(r) = T_S + \frac{q}{4k}\left(R^2 - r^2\right) \tag{7}$$

The maximum temperature occurs at the center of the cell. So, put $r = 0$, $T(0) = T_{\text{Max}}$

$$T_{\text{Maximum}} = T_S + \frac{q}{4k} R^2 \tag{8}$$

2.3 | Heat Transfer Analysis of Battery Pack

Figure 2 depicts the top view of the battery pack with the air flow from the inlet and outlet ends of the battery pack. When the air externally flows around the cell, the maximum velocity of air occurs between the cells. The maximum velocity of flow in between the cells is given by the following relation:

$$V_{\text{Max}} = \frac{y}{x - D} V \tag{9}$$

where x and y are the longitudinal and transverse distances between the center of the cell. V is the velocity of the inlet air, and V_{Max} is the maximum velocity air passes between the cell surface.

The Equation (10) is used to calculate the Reynolds number.

$$Re = \frac{\rho V_{\text{Max}} D}{\mu} \tag{10}$$

The Equation (11) is used to calculate the Nusselt number.

$$Nu = 0.27\left(Re^{0.63}\right)\left(\text{Pr}^{0.36}\right) \tag{11}$$

The Equation (12) is used to calculate the heat transfer coefficient.

$$h = \frac{\text{Nuk}}{D} \tag{12}$$

As per the First Law of thermodynamics

$$Q_g = Q_{CV} + Q_{\text{Air}} \tag{13}$$

$$Q_{CV} = Q_g - Q_{\text{Air}} \tag{14}$$

where Q_{CV} is the heat trapped inside the control volume, Q_g is the heat generated inside the cells, and Q_{Air} is the heat transferred by the cell to the air.

$$Q_{CV} = q \times v - m_{C_p}\left(T_2 - T_1\right) \tag{15}$$

where q is the heat generation (W/m^3), v is the volume of the cell (m^3), m is the mass flow rate of air (kg/s), C_p is the specific heat of air (J/kgK). The trapped heat inside the control volume enhances the temperature of the cells.

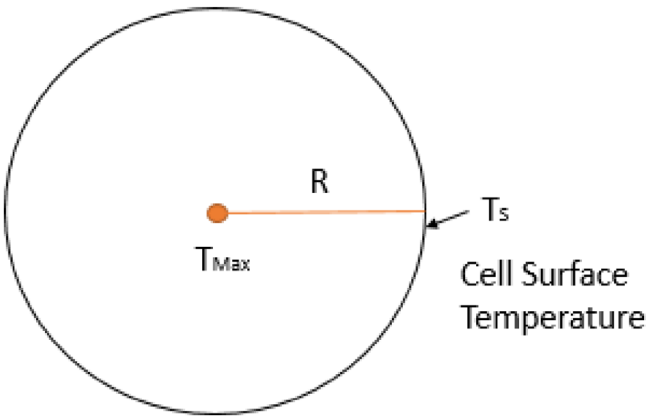

FIGURE 1 | Location of surface and maximum temperature in the cell.

2.4 | Description of the Properties of the Copper Foam

The copper foam is a porous structure made of copper material in which copper material is separated in the form of the pores. Around the pores, the material is interconnected. It works as a good conductor of heat and current in the form of a foam structure. In the advantageous form, it has a lower density and higher surface area. Due to the porous nature, the thermal and physical properties of the copper foam are different than the copper and calculated as the same method proposed by [28, 29].

The pore diameter is calculated by following formula.

$$d_p = \frac{0.0254}{w} \tag{16}$$

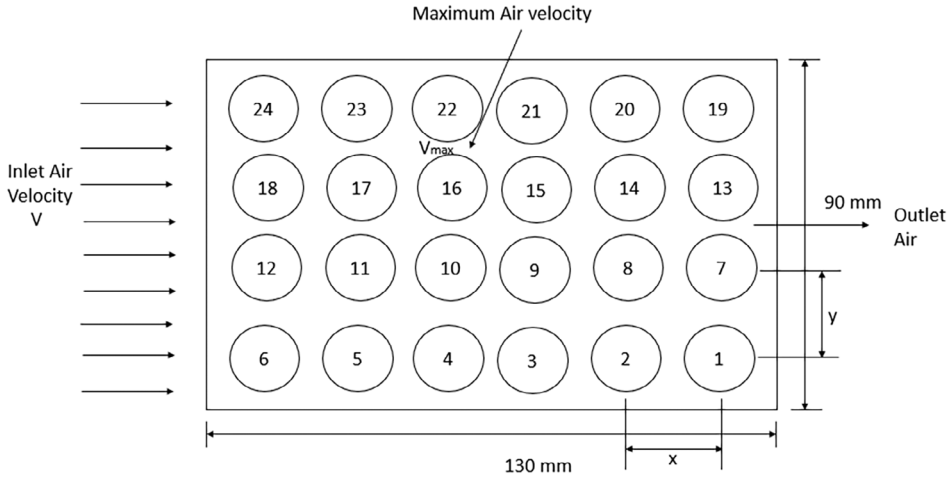

FIGURE 2 | Schematic representation of cells in battery pack.

where w is the pore density (PPI).

The ligament diameter is calculated in terms of the pore diameter.

$$d_L = \frac{1.18 d_p \sqrt{\frac{1-\epsilon}{3\pi}}}{1 - e^{\frac{(1-\epsilon)}{0.04}}} \tag{17}$$

The following formula calculates the permeability of the copper foam

$$K = 0.00073(1-\varepsilon)^{-(0.224)} \left(\frac{d_L}{d_p}\right)^{-1.11} d_p^2 \tag{18}$$

The effective thermal conductivities of the PCM and the copper foam have been calculated using empirical relations.

$$\lambda_{PE} = \frac{\lambda_{LPCM}}{\sqrt{2}} \left[\frac{4\theta}{4 - 2e^2 - \pi\theta(1-e)} + \left(\frac{e-2\theta}{2-e^2}\right) + \left(\frac{1-\sqrt{2e}}{\sqrt{2}-\pi\theta^2}\right) + \left(\frac{2e}{4-\theta^2}\right) \right]^{-1} \tag{19}$$

$$\lambda_{SE} = \frac{\lambda_{MF}}{\sqrt{2}} \left[\frac{4\theta}{2e^2 + \pi\theta(1-e)} + \left(\frac{e-2\theta}{e^2}\right) + \left(\frac{1-\sqrt{2e}}{\pi\theta^2}\right) + \left(\frac{2}{e}\right) \right]^{-1} \tag{20}$$

where θ is calculated by following the empirical relation

$$\theta = \sqrt{\left(\frac{2\sqrt{2} - 1.5e^3 - 2\sqrt{2\varepsilon}}{\pi - 2\sqrt{2e} - e}\right)} \tag{21}$$

where e is 0.33, it depends on the radius of the atomic structure and the side of the unit cell.

In this analysis, the porosity of the copper foam is 90% so that $\varepsilon = 0.9$.

Calculate θ from Equation (21)

$$\theta = 0.43$$

Now calculate the effective thermal conductivity of the copper foam by Equation (20) in which λ_{MF} is 387.6 W/m k Now the effective value of the thermal conductivity of copper foam is

$$\lambda_{SE} = 69.72\,\mathrm{W/mk}$$

3 | Design of Battery Pack for the Simulation Analysis

Figure 3 illustrates the dimensions of the battery container, which was simulated in ANSYS 18.1 Fluent. Figure 3a depicts the battery pack design modeler geometry with 28 cells. The length, width, and height of the battery pack are 130 mm × 90 mm × 70 mm, respectively. The location of the cells from the left side of the battery pack is shown in Figure 3b. The inlet faces of the battery pack shown in Figure 3c consist of 63 holes of 5 mm diameter. The single outlet is provided on the rightmost face of the battery pack, which has a diameter of 50 mm as defined in Figure 3d. Figure 3e shows the meshing for the air cooling, which requires the inlet, outlet, and the fluid volume of the air. The PCM cooling geometry requires no inlet and outlet, and the space among the lithium-ion cells represents the fluid domain of the PCM as represented in Figure 3f. The total number of nodes and elements in control volumes is 240 069 and 400 219, respectively, as shown in Figure 3e–f, the size of the element is selected to be 0.5 mm. The mesh quality has been tested by several parameters, like skewness, element quality, and orthogonality. Skewness represents how close a mesh is to the ideal mesh. The high skewness value shows the mesh's poorest quality, as a low skewness between 0 to 0.95 represents excellent mesh quality. Figure 3e–f shows that the mesh skewness between 0 and 0.29 represents the excellent quality of the mesh. The orthogonality is also a parameter that measures the quality of the mesh. It is just the opposite of the skewness; the high value of the orthogonality represents an excellent mesh. The value of the orthogonality of the mesh that lies between 0.15–1 gives the acceptable mesh quality. Figure 3e–f gives the mesh quality in the 0.21–0.9988 range, representing an accepted mesh orthogonality.

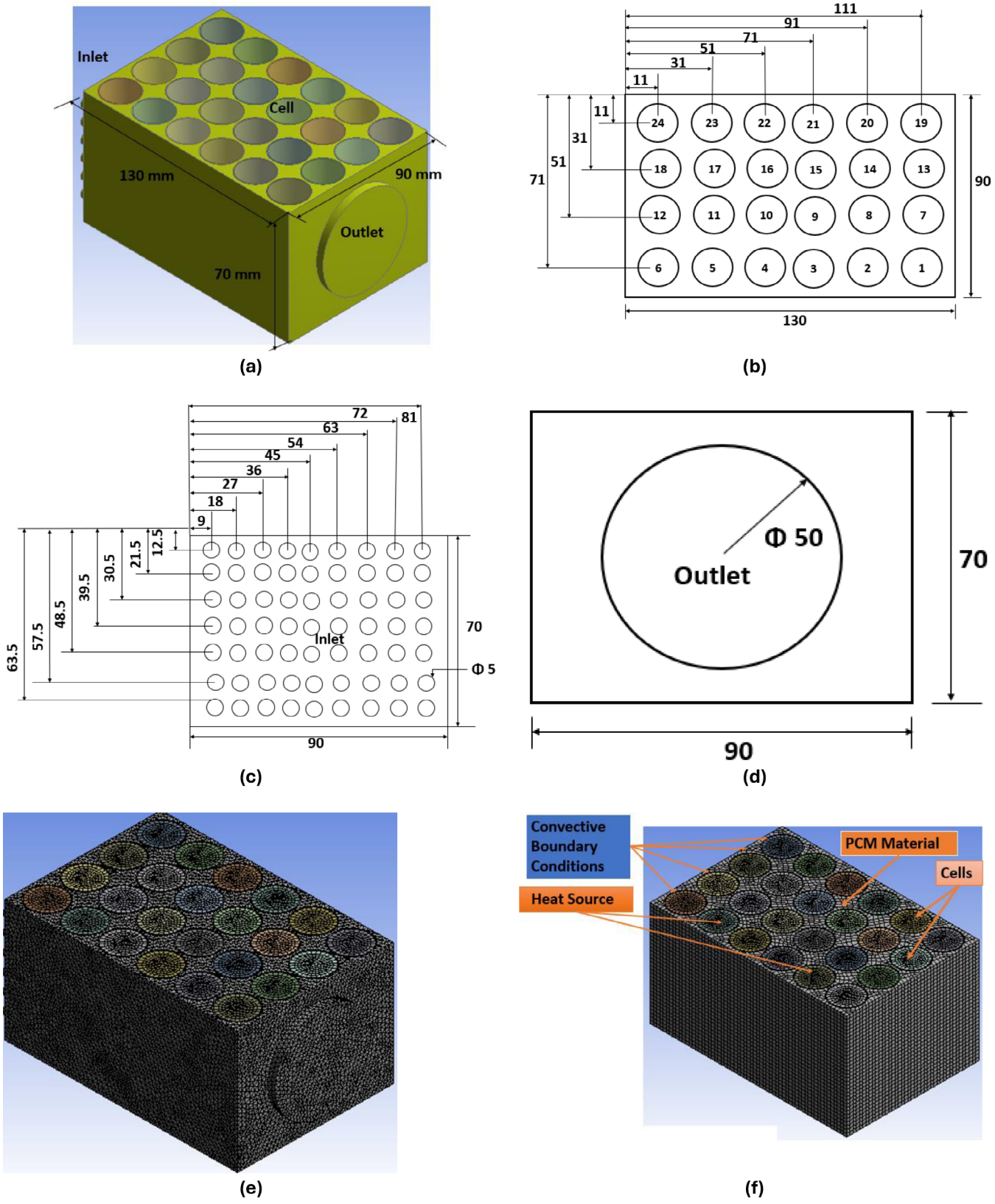

FIGURE 3 | Geometry and meshing of the battery pack. (a) Geometry of the cells in the container, (b) top view of the cells and container, (c) inlet for flow of air, (d) outlet of the container, (e) meshing on the geometry, and (f) meshing on the PCM material-cooled battery pack.

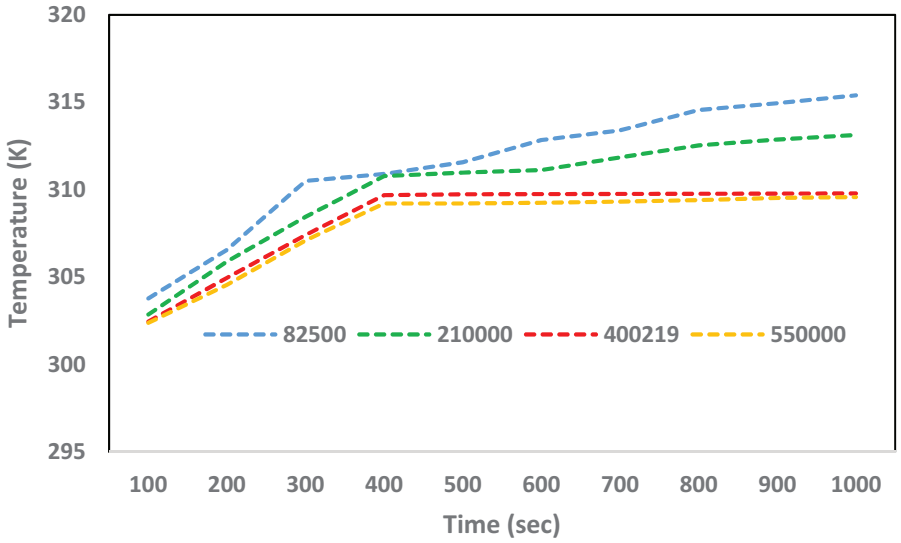

FIGURE 4 | Graphical representation of grid independence TEST.

TABLE 2 | Properties of PCM materials [30, 36].

S. no.	Parameters	n-Eicosane		Paraffin wax		Copper (foam)	Battery cell
		Solid	Liquid	Solid	Liquid		
1	Thermal conductivity (W/m K)	0.423	0.146	—	0.2	387.6	3
2	Latent heat (kJ/kg)	248	—	—	174	—	—
3	Heat capacity (kJ/kg K)	1.926	2.4	—	2.0	0.386	0.3
4	Density (kg/m^3)	910	769	880	760	8900	2720
5	Solidus temperature (K)	309.55	—	—	311.15	—	—
6	Liquidus temperature (K)	309.65	—	—	316.15	—	—

TABLE 3 | Heat generation at various charging rates in a Lithium-ion cell.

Charging rates	1C	2C	3C	5C
Heat generation (W/m^3)	10447	41788	94024	412200

3.1 | Assumptions and Boundary Conditions

This section lists the assumptions made during the numerical simulation.

1. The heat generation inside the cell is assumed to be uniform.
2. The cell and air properties are assumed to be constant.
3. The thermal contact resistance is neglected.
4. The cell thermal conductivity has orthogonal and anisotropic properties.
5. The phenomenon of radiation on the surface is neglected.
6. The physical properties of the PCM material differ in the solid and liquid phases and are separately defined. But the properties of PCM are independent of temperature.

In the air-cooling simulation, the inlet velocity and outlet pressure boundary conditions are applied at the control volume's inlet and outlet. Heat transfers between the air and the cell surface are mainly caused by convection; the assumed heat transfer coefficient in this analysis is 5.7 W/m^2 k [30]. The heat generation inside the cell is considered constant at a fixed charging for simplifying the numerical simulation. The n-eicosane is the stable paraffin-based PCM; it has been chosen due to its low cost and stability. Moreover, the copper foam used has the 90% porosity selected based on the work presented by Heyhat et al. [31]. The air properties like viscosity, density, specific heat, and thermal conductivity remain constant with temperature. The PCM cooling boundary conditions are shown in Figure 3f. The battery pack is made of aluminum, which loses heat by convection in the atmosphere. The PCM material is considered to be a fluid, so convective boundary conditions are applied at the surface of the cell. The battery cells also work as the heat source, with a constant heat generation applied to the cells. The PCM material is considered to be isotropic; the cell resistance is neglected, so all heat generated inside the cells is utilized to melt the PCM material. For handling the

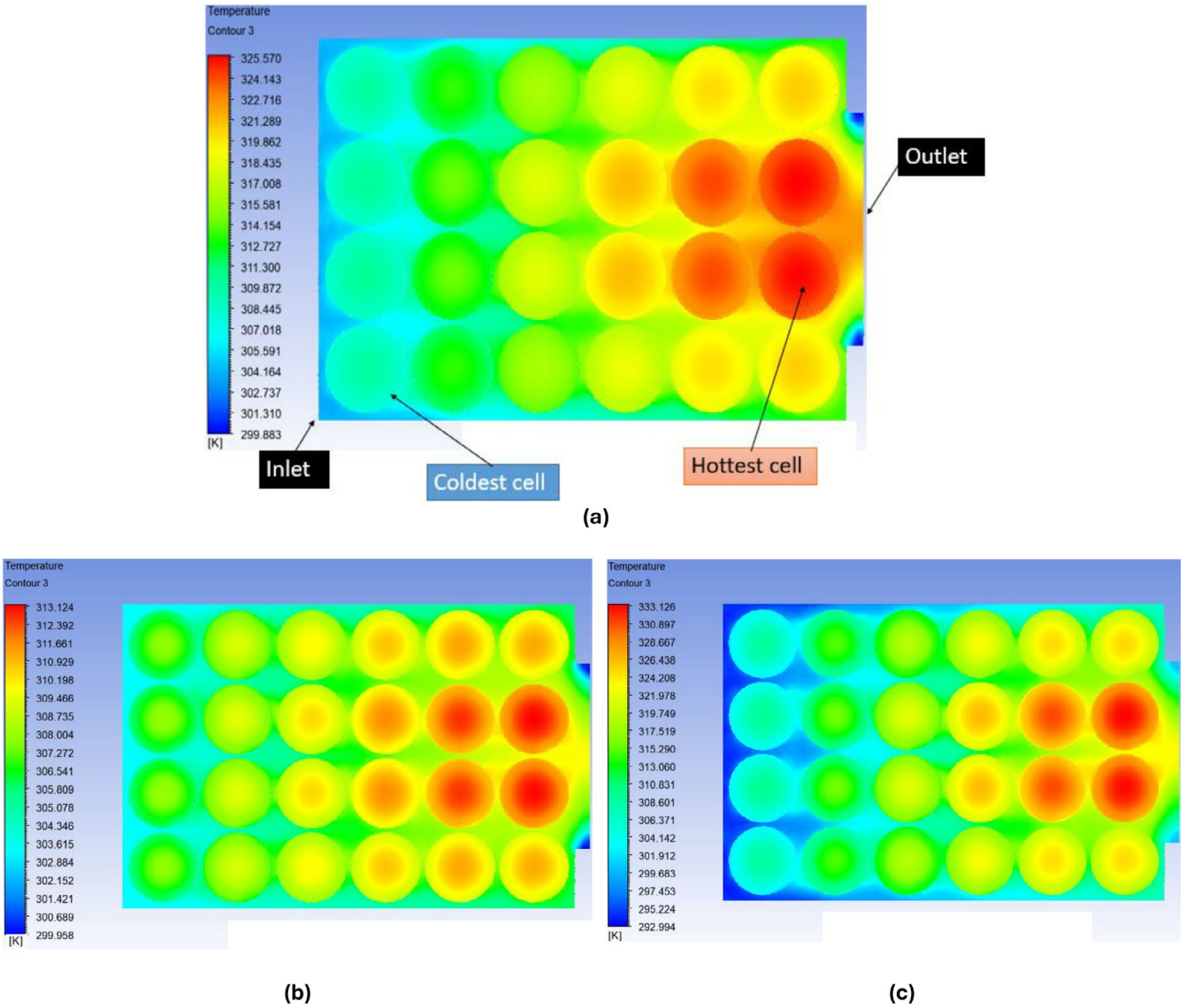

FIGURE 5 | Temperature plots of the battery pack at different values of heat generation, inlet velocity and temperature. (a) Temperature contour at $q = 24\,375\,\mathrm{W/m^3}$, $V = 0.5\,\mathrm{m/s}$, $T_{\mathrm{Inlet}} = 30°\mathrm{C}$. (b) Temperature contour at $q = 24\,375\,\mathrm{W/m^3}$, $V = 1.5\,\mathrm{m/s}$, $T_{\mathrm{Inlet}} = 30°\mathrm{C}$. (c) Temperature contour at $q = 73\,125\,\mathrm{W/m^3}$, $V = 1\,\mathrm{m/s}$, $T_{\mathrm{Inlet}} = 20°\mathrm{C}$.

PCM material, the solidification-melting has been selected in the general model at the transient state.

3.2 | Grid Independent Test

The main purpose of this test is to refine the mesh size for the simulation. The mesh should be fine enough to give accurate results, since an extra fine mesh could increase the computational cost and time. The optimal mesh maintains the accuracy, efficiency, and reliability of the solution at minimum computational time and cost. The element size selected for the analysis is 2, 1.5, 1, and 0.5 mm, corresponding to the element sizes 82 500, 210 000, 320 000, and 400 219. Figure 4 depicts the variation of the maximum cell temperature with time of the simulation at dissimilar mesh numbers. Initially, when the number of elements changed from 82 500 to 210 000, the maximum cell temperature reduced, and the reduction in temperature was large enough. Furthermore, increasing the mesh numbers from 210 000 to 400 219 will again reduce the temperature, indicating that the solution will continue to converge. But if the mesh number changes from 400 219 to 550 000, the marginal temperature variation is noted (0.11%), so the selected mesh element is 400 219.

3.3 | Governing Equations

3.3.1 | Air Cooling

The governing equations are basic equations that rule the fluid flow and heat transfer phenomena. Three basic equations, conservation equations, model the flow, and the equations are computationally solved to determine the distinct contour plot of the velocity, temperature, and pressure. So, following are the basic equations:

- Conservation of mass equation.

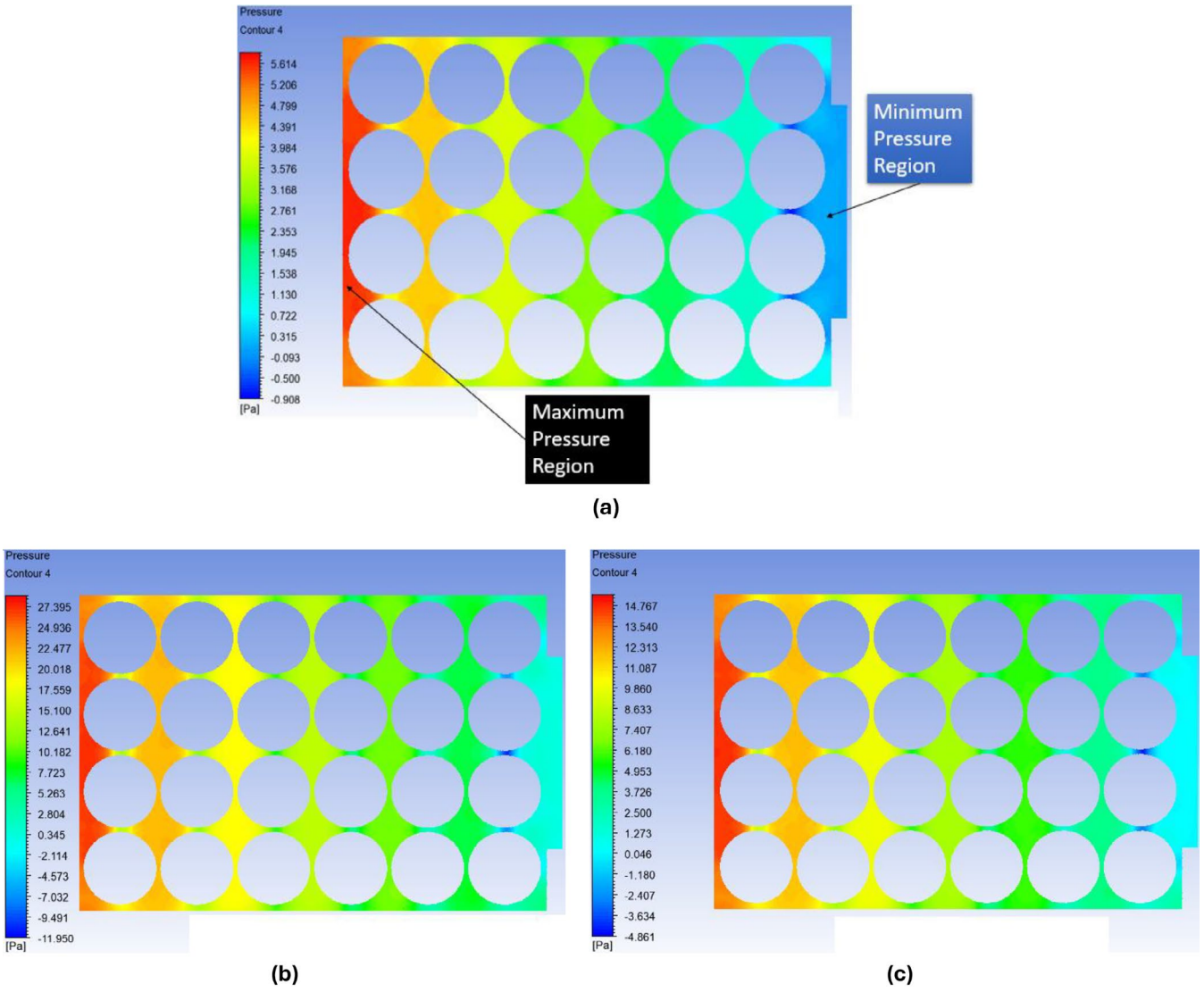

FIGURE 6 | Pressure contour of the battery pack. (a) Pressure contour at $q = 24\,375\,\mathrm{W/m^3}$, $V = 0.5\,\mathrm{m/s}$, $T_{\mathrm{Inlet}} = 30°\mathrm{C}$. (b) Pressure contour at $q = 24\,375\,\mathrm{W/m^3}$, $V = 1.5\,\mathrm{m/s}$, $T_{\mathrm{Inlet}} = 30°\mathrm{C}$. (c) Pressure contour at $q = 73\,125\,\mathrm{W/m^3}$, $V = 1\,\mathrm{m/s}$, $T_{\mathrm{Inlet}} = 20°\mathrm{C}$.

$$\frac{\partial(\rho u)}{\partial x} + \frac{\partial(\rho v)}{\partial y} + \frac{\partial(\rho w)}{\partial z} = 0 \tag{22}$$

- Momentum equation.
  - X-Momentum equation

$$\rho\left(\frac{u\partial u}{\partial x} + \frac{v\partial u}{\partial y} + \frac{w\partial u}{\partial z}\right) = \rho g_x - \frac{\partial P}{\partial x} + \frac{\partial}{\partial x}\left(\frac{2\mu\partial u}{\partial x} + \lambda\overrightarrow{\nabla}.\overrightarrow{V}\right) + \frac{\partial}{\partial y}\left[\mu\left(\frac{\partial u}{\partial y} + \frac{\partial v}{\partial x}\right)\right] + \frac{\partial}{\partial z}\left[\mu\left(\frac{\partial u}{\partial z} + \frac{\partial w}{\partial x}\right)\right] \tag{23}$$

  - Y-Momentum equation

$$\rho\left(\frac{u\partial v}{\partial x} + \frac{v\partial v}{\partial y} + \frac{w\partial v}{\partial z}\right) = \rho g_y - \frac{\partial P}{\partial y} + \frac{\partial}{\partial x}\left[\mu\left(\frac{\partial v}{\partial x} + \frac{\partial u}{\partial y}\right)\right] + \frac{\partial}{\partial y}\left[2\mu\left(\frac{\partial y}{\partial y} + \lambda\overrightarrow{\nabla}.\overrightarrow{V}\right)\right] + \frac{\partial}{\partial z}\left[\mu\left(\frac{\partial v}{\partial z} + \frac{\partial w}{\partial y}\right)\right] \tag{24}$$

  - Z-Momentum equation

$$\rho\left(\frac{u\partial w}{\partial x} + \frac{v\partial w}{\partial y} + \frac{w\partial w}{\partial z}\right) = \rho g_z - \frac{\partial P}{\partial z} + \frac{\partial}{\partial x}\left[\mu\left(\frac{\partial w}{\partial x} + \frac{\partial u}{\partial z}\right)\right] + \frac{\partial}{\partial y}\left[\mu\left(\frac{\partial v}{\partial z} + \frac{\partial w}{\partial y}\right)\right] + \frac{\partial}{\partial z}\left[\frac{2\mu\partial w}{\partial z} + \lambda\overrightarrow{\nabla}.\overrightarrow{V}\right] \tag{25}$$

3.3.2 | Energy Equation

$$\rho C_P\left(\frac{u\partial T}{\partial x} + \frac{v\partial T}{\partial y} + \frac{w\partial T}{\partial Z}\right) = \beta T\left(\frac{u\partial P}{\partial x} + \frac{v\partial P}{\partial y} + \frac{w\partial P}{\partial z}\right) + \overrightarrow{\nabla.(k\overrightarrow{\nabla T})} + \phi \tag{26}$$

where u, v, and w are the velocities of air corresponding to x, y, and z directions, and β is the coefficient of volume expansion. The term ϕ is known as viscous dissipation. It is represented by the following Equation [32].

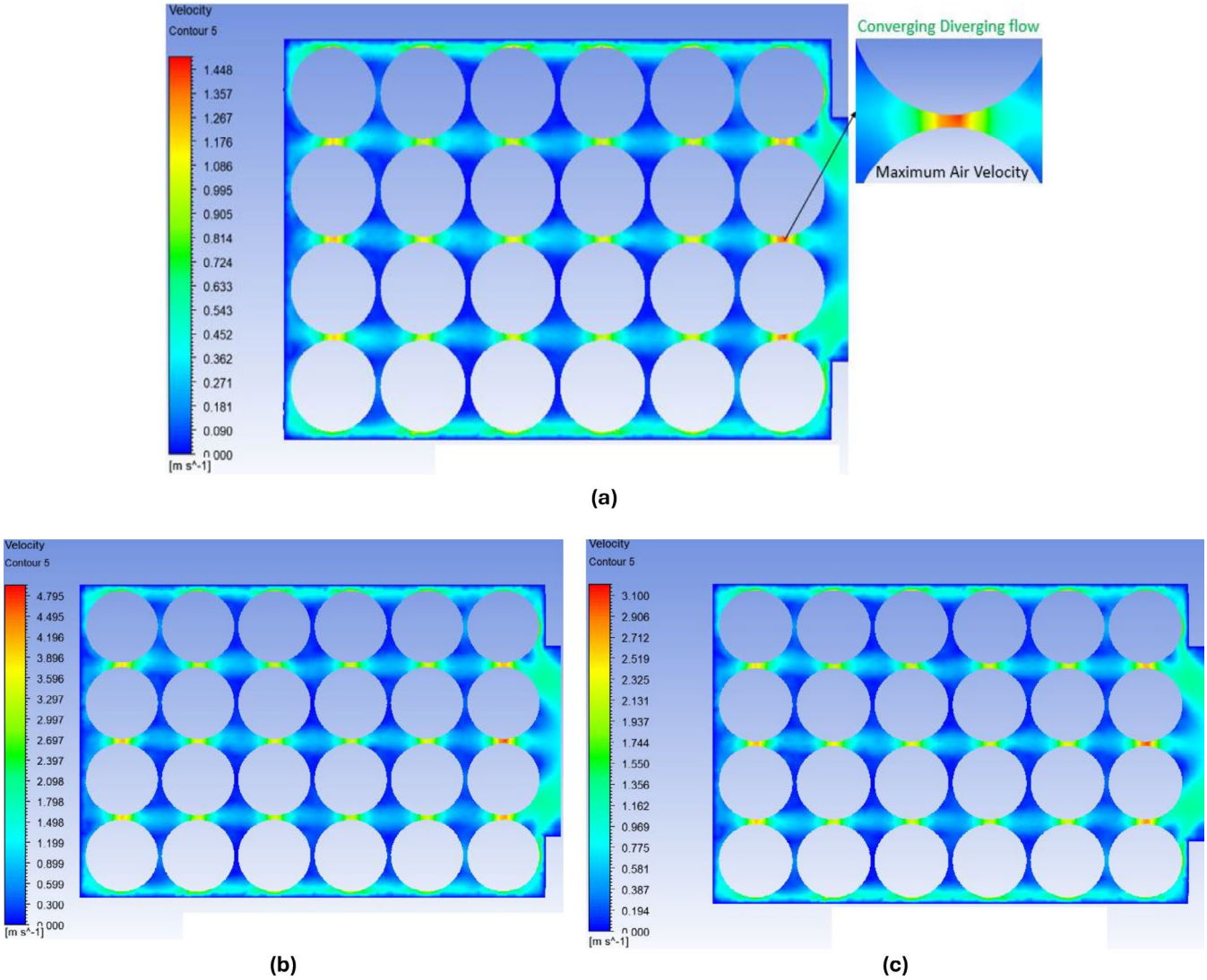

FIGURE 7 | Velocity contour of the battery pack at different conditions. (a) Velocity contour at $q = 24\,375\,\mathrm{W/m^3}$, $V = 0.5\,\mathrm{m/s}$, $T_{\mathrm{Inlet}} = 30°\mathrm{C}$. (b) Velocity contour at $q = 24\,375\,\mathrm{W/m^3}$, $V = 1.5\,\mathrm{m/s}$, $T_{\mathrm{Inlet}} = 30°\mathrm{C}$. (c) Velocity contour at $q = 73\,125\,\mathrm{W/m^3}$, $V = 1\,\mathrm{m/s}$, $T_{\mathrm{Inlet}} = 20°\mathrm{C}$.

$$\phi = 2\mu\left[\left(\frac{\partial u}{\partial x}\right)^2 + \left(\frac{\partial v}{\partial y}\right)^2 + \left(\frac{\partial w}{\partial z}\right)^2\right] + \mu\left[\left(\frac{\partial v}{\partial x} + \frac{\partial u}{\partial y}\right)^2 + \left(\frac{\partial v}{\partial z} + \frac{\partial w}{\partial y}\right)^2 + \left(\frac{\partial u}{\partial z} + \frac{\partial w}{\partial x}\right)^2\right] + \lambda\left(\frac{\partial u}{\partial x} + \frac{\partial v}{\partial y} + \frac{\partial w}{\partial z}\right)^2 \quad (27)$$

3.3.3 | Turbulence Model

The model selection depends on the accuracy of the results. In this SAH model analysis, the k-ε (two-equation) model has been used for determining the velocity and pressure distribution with good accuracy [32].

3.3.4 | K-ε Model

In the k-ε model, the k signifies the kinetic energy of turbulence, and ε denotes the turbulence dissipation rate.

The velocity and length scale are defined in terms of the k and ε by the following equation [33].

$$v = k^{\frac{1}{2}} \quad (28)$$

$$l = \frac{k^{\frac{3}{2}}}{\varepsilon} \quad (29)$$

So following are the two equations representing in the term of k and ε [33].

$$\frac{\partial(\rho k)}{\partial(t)} + \mathrm{div}(\rho k U) = \mathrm{div}\left[\frac{\mu_t}{\sigma_t}\,\mathrm{grad}\,k\right] + 2\mu_t S_{ij}.S_{ij} - \rho\varepsilon \quad (30)$$

$$\frac{\partial(\rho\varepsilon)}{\partial(t)} + \mathrm{div}(\rho\varepsilon U) = \mathrm{div}\left[\frac{\mu_t}{\sigma_\varepsilon}\mathrm{grad}\,k\right] + C_{1\varepsilon}\left(\frac{\varepsilon}{k}\right)2\mu_t S_{ij}.S_{ij} - \frac{C_{2\varepsilon}\rho\varepsilon^2}{k} \quad (31)$$

where μ_t represents the eddy viscosity by following equations:

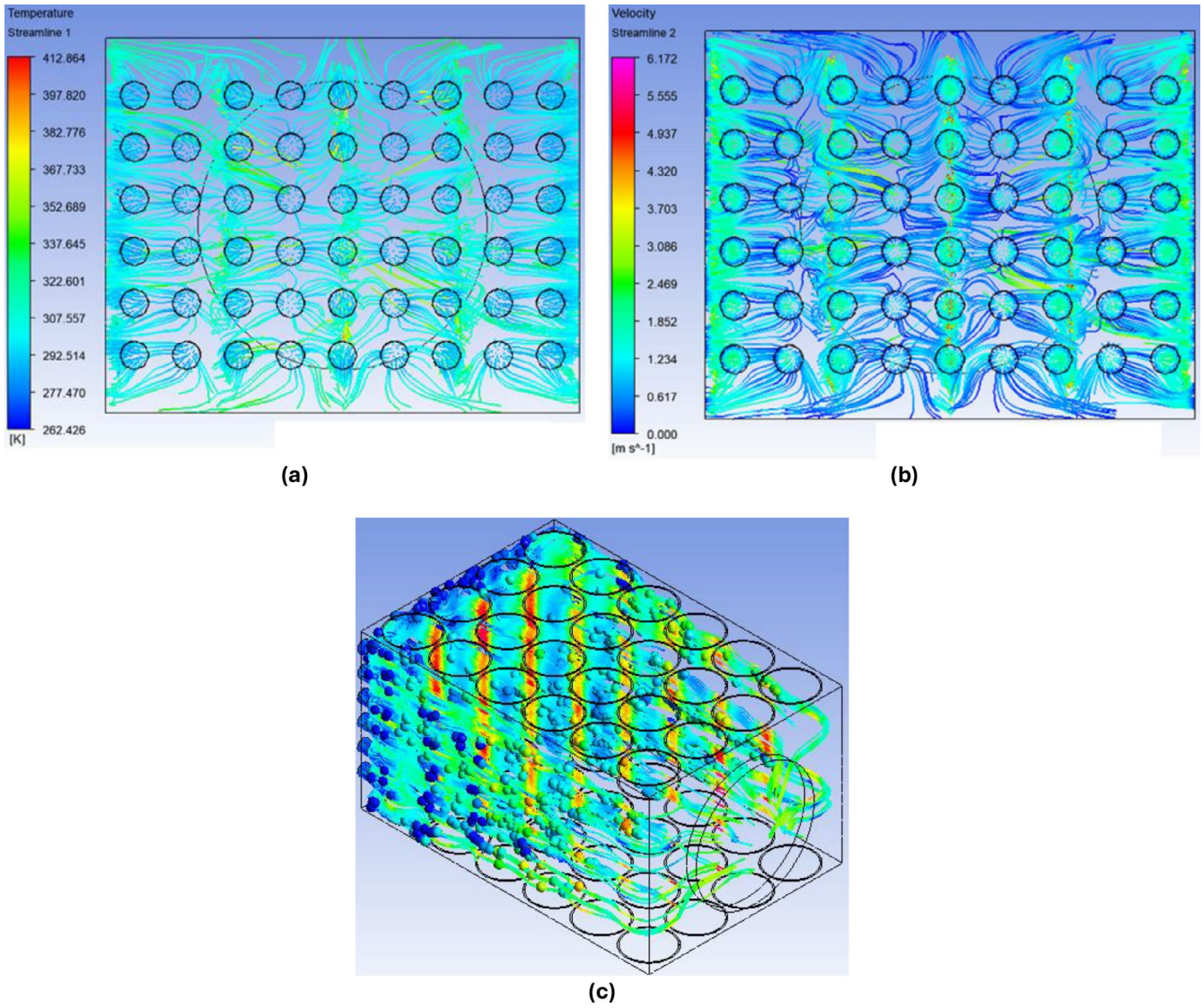

FIGURE 8 | Temperature and velocity streamlines plot. (a) Temperature streamlines at $q = 412\,200\,\mathrm{W/m^3}$, $V = 2\,\mathrm{m/s}$, $T_{\mathrm{Inlet}} = 10°\mathrm{C}$. (b) Velocity streamlines at $q = 412\,200\,\mathrm{W/m^3}$, $V = 2\,\mathrm{m/s}$, $T_{\mathrm{Inlet}} = 10°\mathrm{C}$. (a) 3D streamlines plot inside the battery pack.

$$\mu_t = \frac{\rho C_\mu k^2}{\varepsilon} \tag{32}$$

The value of five constants used in the above equation is represented below [33].

$$C_\mu = 0.09, \sigma_K = 1.00, \sigma_\varepsilon = 1.30, C_{1\varepsilon} = 1.44, \text{and } C_{2\varepsilon} = 1.92$$

3.3.5 | PCM Material

The PCM cooling is different from air cooling. For dealing with the PCM material, the solidification and melting model is given in Fluent to know the melting behavior. The natural convection dominates as associated with conduction in the phase change material. The strength of the natural convection depends on the change in density due to temperature, which is represented by the Boussinesq equation [34].

$$\rho_T = \frac{\rho}{\left[\beta\left(T - T_{\mathrm{Liquid}}\right) + 1\right]} \tag{33}$$

The continuity equation is represented based on conservation of mass as follows:

$$\frac{\partial \rho}{\partial t} + \nabla . \left(\rho \overrightarrow{V}\right) = 0 \tag{34}$$

The momentum equation based on Newton's second law is represented as

$$\frac{\partial (\rho V)}{\partial t} + \nabla . (\rho \overrightarrow{V}\,\overrightarrow{V}) = \left(\mu \nabla^2 \overrightarrow{V} - \nabla p + \rho \vec{g}\right) + \vec{S} \tag{35}$$

The $\vec{S}$ in above equation represents the source term. It is further represented as.

$$\vec{S} = -A_{\mathrm{Mushy}} \left[\frac{(1-\lambda)^2}{\lambda^3 + \varepsilon}\right] \times \overrightarrow{V} \tag{36}$$

where A_{Mushy} is represents the constant of the mushy zone, it is used to model the PCM melting in between the solid and liquid phase. Its value lies in the range of 10^4–$10^7\,\mathrm{kg/m^3 s}$. The ε is constant, its value assumed to be 0.001 [35].

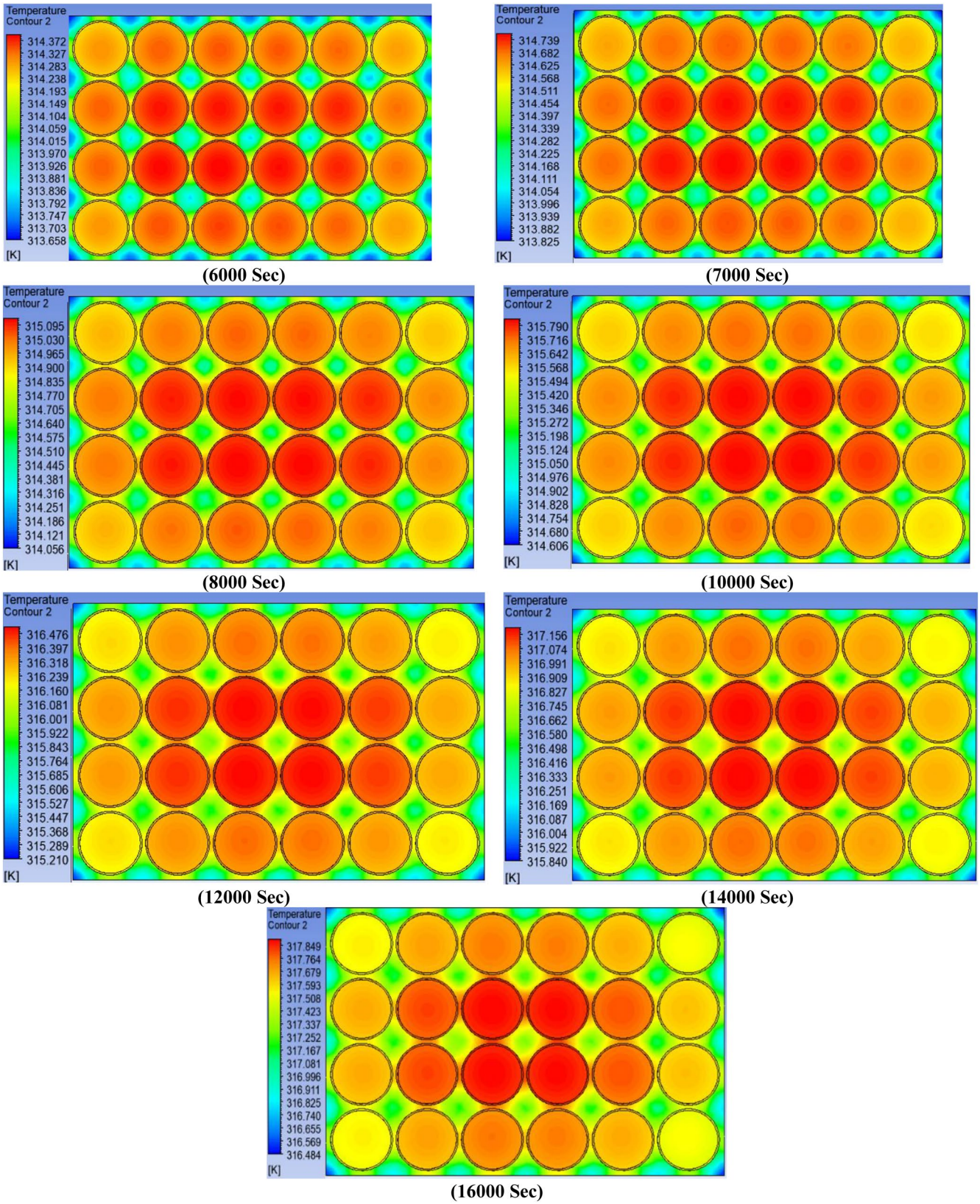

FIGURE 9 | Temperature contour of battery pack at different times in 1 C charging rate.

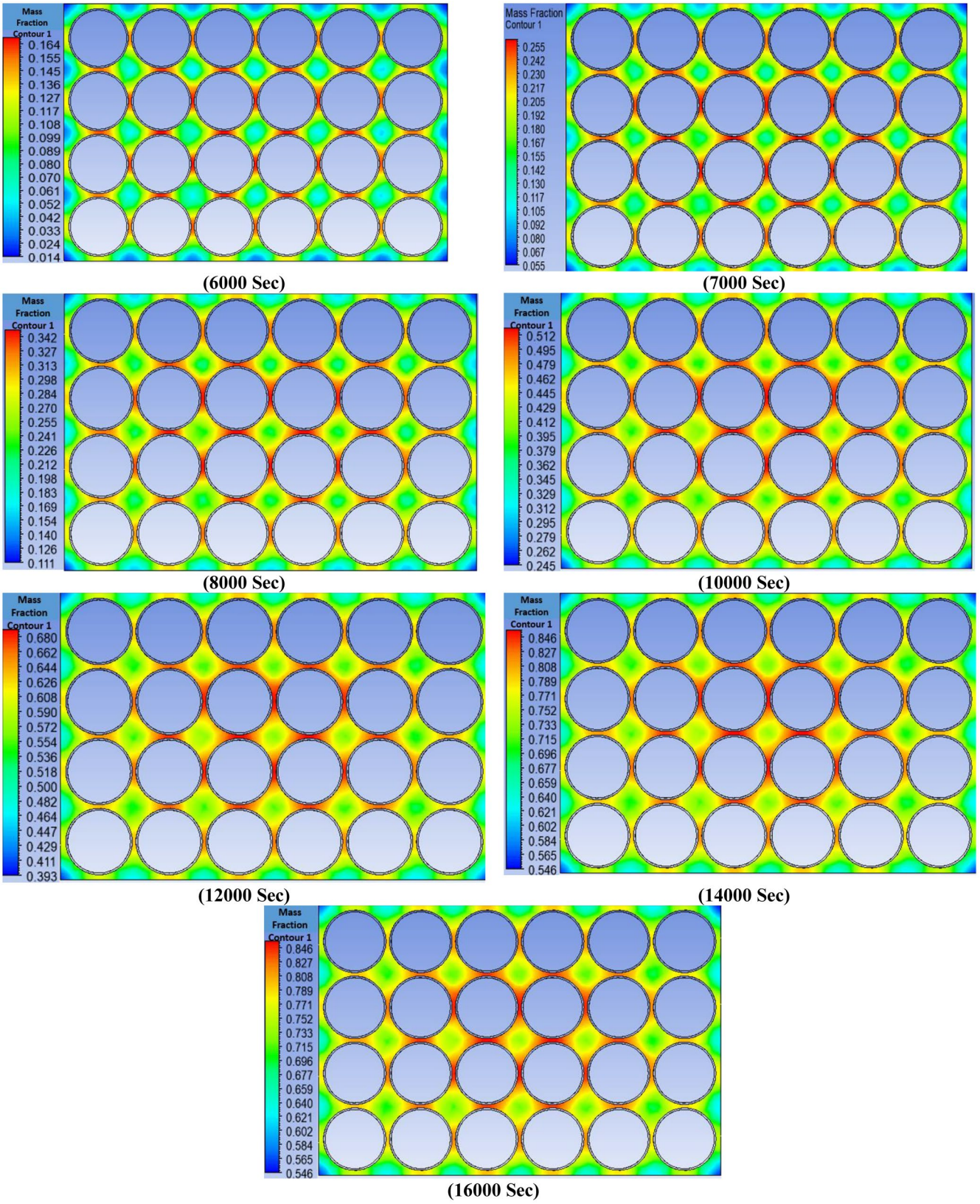

FIGURE 10 | Mass fraction contour of the battery pack at 1 C charging at different times.

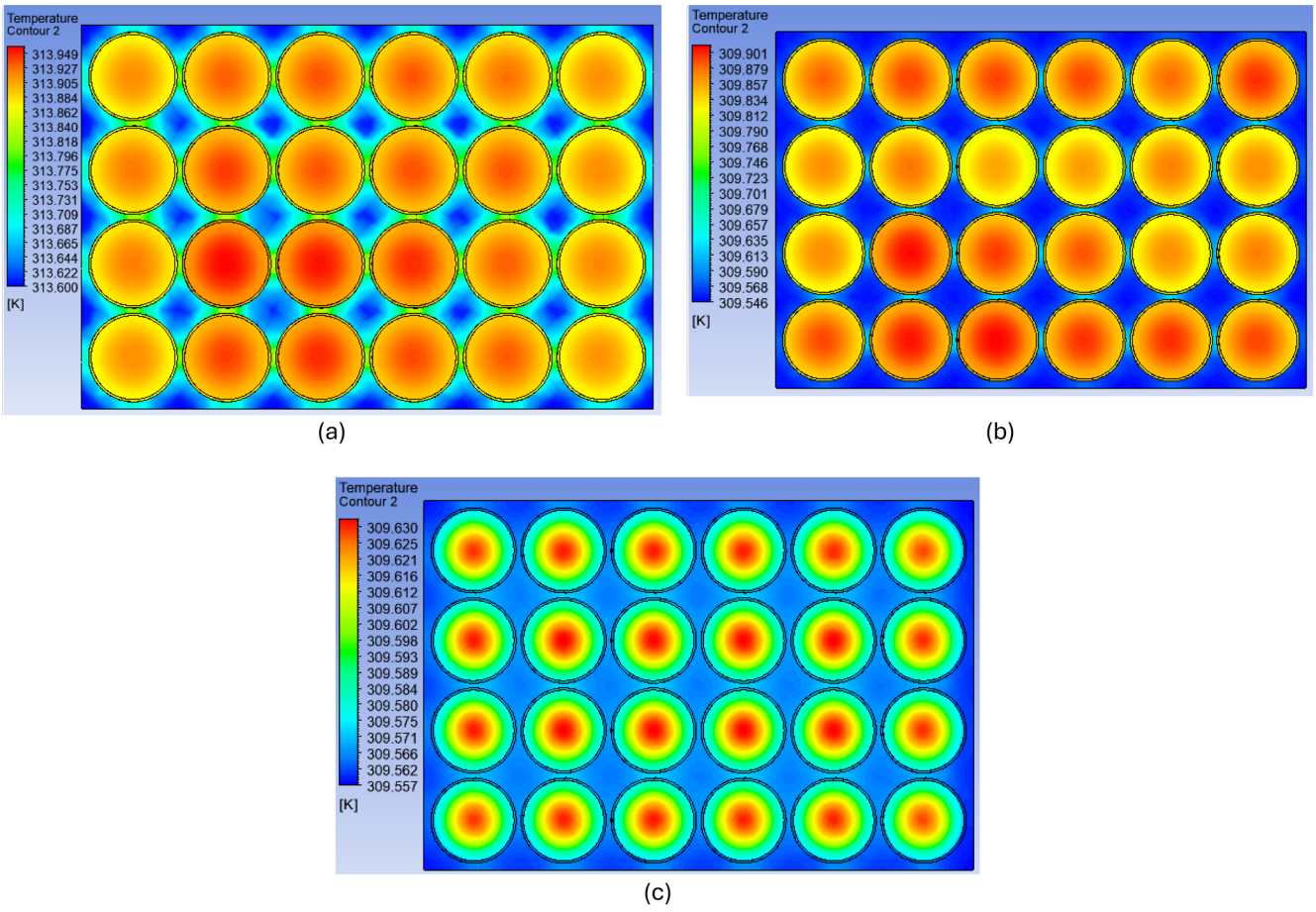

FIGURE 11 | Temperature contour of paraffin wax, n-eicosaine, and copper foam at 5000 s at 1 C charging.

The energy equation is represented as follows:

$$\frac{\partial(\rho H)}{\partial t} + \nabla . \left(\rho \vec{V} H\right) = \nabla . (k \nabla T) \tag{37}$$

where H represents the total enthalpy.

$$H = h + \delta H \tag{38}$$

Sensible enthalpy is further elaborated as follows:

$$h = h_{\text{Ref}} + C_P \int_{T_{\text{Ref}}}^{T} dT \tag{39}$$

The following equation can determine the latent heat.

$$\delta H = \sum_{i=1}^{n} \lambda_i h_{\text{sf}} = \lambda L \tag{40}$$

L is the latent heat, λ is the liquid fraction. For the solid phase $\lambda = 0$ and liquid phase $\lambda = 1$. The value of the λ varies between 0 and 1. If T_S is the solidus and T_L is the liquidus temperature, then λ can be represented by the following equations.

$$\lambda = 0 \qquad T < T_S \tag{41}$$

$$\lambda = \frac{T - T_S}{T - T_L} \qquad T_S < T < T_L \tag{42}$$

$$\lambda = 1 \qquad T > T_L \tag{43}$$

The following conduction equation will be used for the solid PCM material in the cylindrical coordinate system.

$$\frac{\partial h}{\partial t} = k_S \left(\frac{\partial^2 T}{\partial r^2} + \left(\frac{1}{r}\right)\left(\frac{\partial T}{\partial r}\right) + \left(\frac{1}{r^2}\right) \times \left(\frac{\partial^2 T}{\partial \emptyset^2}\right)\right) \tag{44}$$

$$\frac{\partial h}{\partial t} = k_L \left(\frac{\partial^2 T}{\partial r^2} + \left(\frac{1}{r}\right)\left(\frac{\partial T}{\partial r}\right) + \left(\frac{1}{r^2}\right) \times \left(\frac{\partial^2 T}{\partial \emptyset^2}\right)\right) \tag{45}$$

The k_S and k_L show the solid and liquid PCM thermal conductivity, respectively, given in Table 2. Table 3 represents the heat generation at various charging rates.

4 | Results and Discussion

4.1 | Simulation Results

Figure 5 represents the temperature contour at different values of input factors, namely heat generation, inlet velocity, and temperature. Figure 5a depicts the cells near the inlet section representing the minimum temperature, and the cells away from the inlet show the maximum temperature and damage first due to temperature stroke. The same temperature variation from inlet to outlet is seen inside the battery pack in all conditions of variations of input parameters, as represented in Figure 5b,c.

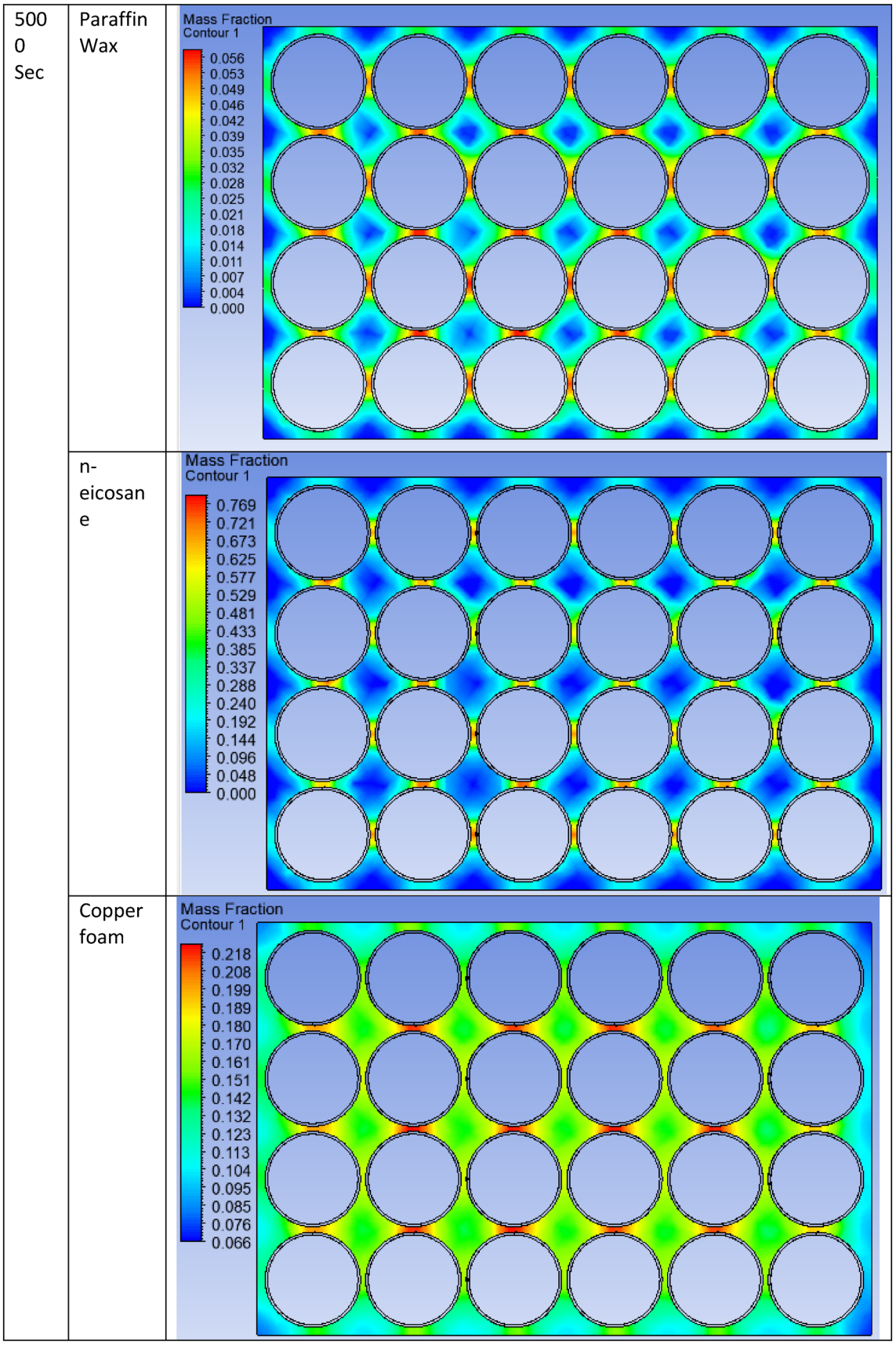

FIGURE 12 | Liquid fraction of various PCM materials at 5000 s at 1 C charging.

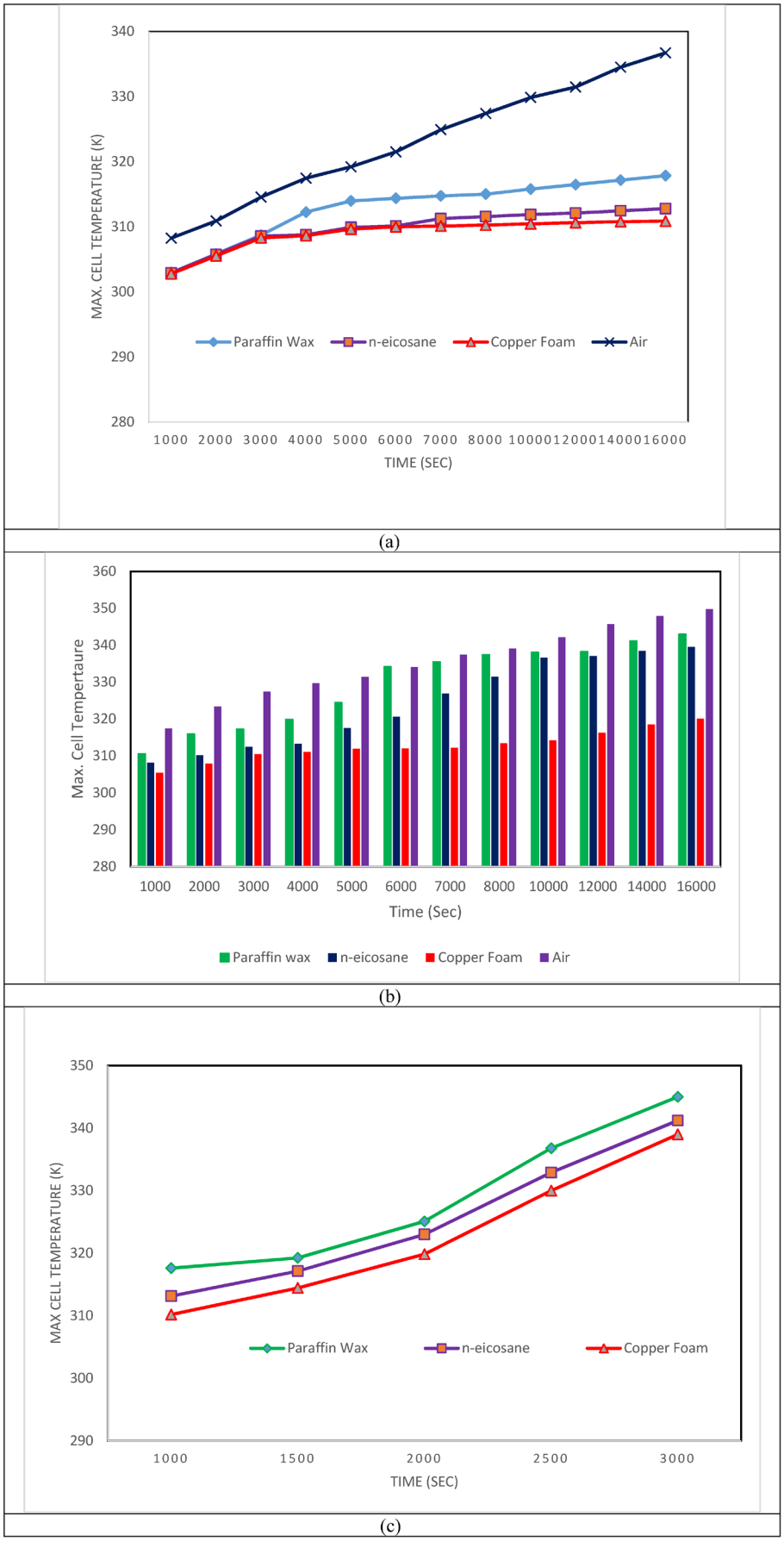

FIGURE 13 | Graphical plots of the maximum cell temperature at different time steps and charging rates. (a) Cell temperature at 1 C charging rate. (b) Cell temperature at 2 C charging rate. (c) Cell temperature at 3 C charging rate.

As the air inlet velocity enhances from 0.5 to 1.5 m/s, the maximum temperature of the cells reduces from 325.57 to 313.124 K, as represented in Figure 5a,b. Figure 5b,c has the maximum cell temperature of 313.124 and 333.126 K if the heat generation increases from 24 375 to 73 125 W/m^3.

Figure 6 represents the pressure drop inside the battery pack due to form and skin friction drag generated by the lithium-ion cells. Figure 6a clearly shows that the minimum pressure occurs near the outlet end of the pack and the maximum pressure occurs near the inlet face due to direct striking of the air on the surfaces of the cells. The maximum pressure drop occurs to be 5.614 Pa at 0.5 m/s flow velocity. As the air flow velocity increases, then the pressure drop also increases; it is directly proportional to the square of the inlet air velocity and the number of cells inside the battery pack. In Figure 6b,c, the maximum pressure drop occurs to be 27.379 and 14.674 Pa at inlet air velocities of 1.5 and 1 m/s. The effect of the temperature on the pressure is neglected.

It is observed from Figure 7a–c that the air velocity is enhanced inside the battery pack due to satisfying the conservation of the mass equation. It is depicted from Figure 7a that if the inlet air velocity is 0.5 m/s then the maximum air velocity inside the battery pack is 1.448 m/s. The air flow velocity is maximum inside the narrow gap of the cylinder. The air experiences the converging and diverging flow with maximum air velocity as air passes among the cylinders. The enhanced air velocity around the cylindrical surface creates a lot of turbulence and promotes heat transfer to the air.

TABLE 4 | Input variables codes and numerical values.

	Coded level		
Input	**−1**	**0**	**1**
Heat generation (W/m^3)	24 375	48 750	73 125
Air inlet velocity (m/s)	0.5	1.0	1.5
Inlet air temperature (°C)	25	30	35

4.2 | Streamline Plot Air Cooled Battery Pack in *y*–*z* Plane

Figure 8 depicts the temperature and velocity streamlines. Figure 8a depicts the 2D temperature streamline plot at a heat generation of 412 200 W/m^3, an inlet air velocity and an inlet air temperature of 2 m/s and 10°C. These streamlines are shown from the inlet section and moving to the outlet end of the pack. Figure 8b displays the pictorial view of the velocity stream lines from the inlet to the outlet end of the battery pack. The air flow velocity inside the different parts of the battery pack is higher than the inlet air velocity due to air converging among the cell surfaces. Figure 8c shows the 3D streamlines inside the battery pack with the air flow.

5 | Battery Pack Cooled by PCM Material

5.1 | Temperature Contour of Paraffin Wax at Various Time Intervals in 1 C Charging

Figure 9 displays the contour plots of the temperature at various time intervals in 1 C charging rates of the LIB pack under PCM material cooling. In 1 C charging, the time required

TABLE 5 | Total 15 runs on the simulation.

S. no.	Heat generation (W/m^3)	Air inlet velocity (m/s)	Inlet air temperature (°C)	Outlet air temperature (K)	Maximum cell temperature (K)	Pressure drop (Pa)	Cooling efficiency (%)
1	24 375	0.5	30	312.324	325.700	6.522	6.9749
2	24 375	1.5	30	304.834	313.124	39.345	4.1170
3	73 125	1	20	310.029	333.126	19.628	8.4925
4	73 125	1.5	30	311.034	333.423	39.278	6.0099
5	48 750	1	30	311.115	329.678	19.637	6.0705
6	48 750	1.5	20	302.192	313.343	39.308	10.3143
7	24 375	1	40	313.000	326.190	19.612	0.0000
8	73 125	1	40	321.529	352.907	19.634	4.2535
9	48 750	0.5	20	316.472	338.360	6.522	8.7793
10	48 750	1	30	311.115	329.678	19.637	6.0705
11	48 750	1.5	40	313.674	333.165	39.350	0.7563
12	24 375	1	20	300.660	306.408	19.617	11.4603
13	48 750	0.5	40	329.000	357.991	6.525	5.9845
14	73 125	0.5	30	333.195	370.829	6.525	7.5293
15	48 750	1	30	311.115	329.678	19.637	6.0705

TABLE 6 | ANOVA analysis of outlet air temperature (K) and Maximum Cell Temperature (K).

		Air outlet temperature (K)				Maximum cell temperature (K)			
Sources	**df**	**Adj. SS**	**Adj. MS**	***F***	***p***	**Adj. SS**	**Adj. MS**	***F***	***p***
Model	9	1095.51	121.723	57.85	0.0000	4084.07	453.79	126.17	0.0000
Linear	3	977.89	325.963	154.92	0.0000	3792.12	1264.04	351.46	0.0000
q	1	252.77	252.771	120.13	0.0000	1766.05	1766.05	491.04	0.0000
V_{In}	1	438.92	438.917	208.60	0.0000	1245.63	1245.63	346.34	0.0000
T_{In}	1	286.20	286.203	136.32	0.0000	780.44	780.44	216.99	0.0000
Square	3	63.35	21.118	10.04	0.015	137.81	45.94	12.77	0.009
$q \times q$	1	0.04	0.038	0.02	0.899	0.000	0.00	0.00	0.987
$V_{IN} \times V_{IN}$	1	63.01	63.008	29.94	0.003	136.22	136.22	14.29	0.002
$T_{In} \times T_{In}$	1	0.03	0.0002	0.01	0.911	0.01	0.01	42.86	0.971
Two-way interaction	3	54.26	18.088	8.60	0.020	154.14	51.38	0.00	0.007
$q \times V_{IN}$	1	53.81	53.813	25.57	0.004	154.13	154.13	0.00	0.001
$V_{IN} \times T_{In}$	1	0.18	0.176	0.08	0.784	0.0000	0.000	—	1.000
$T_{In} \times q$	1	0.27	0.274	0.13	0.733	0.01	0.01	—	0.962
Error	5	10.52	2.104	—	—	17.98	3.60	—	—
Lack of fit	3	10.52	3.507	—	—	17.98	5.99	—	—
Pure error	2	0.0000	0.0000	—	—	0.00	0.00	—	—
Total	14	1106.03	—	—	—	4102.05	—	—	—

TABLE 7 | ANOVA analysis of pressure drop (pa) and cooling efficiency.

		Pressure drop (Pa)				Cooling efficiency (%)			
Sources	**df**	**Adj. SS**	**Adj. MS**	***F***	***p***	**Adj. SS**	**Adj. MS**	***F***	***p***
Model	9	2191.74	243.53	774 945.74	0.0000	133.581	14.8423	45.61	0.000
Linear	3	2151.25	717.08	2 281 892.34	0.0000	108.249	36.0829	110.88	0.000
q	1	0.000	0.000	0.38	0.563	1.742	1.7419	5.35	0.069
V_{In}	1	2151.25	2151.25	6 845 675.80	0.000	8.142	8.1416	25.02	0.004
T_{In}	1	0.00	0.000	0.84	0.401	98.365	98.3652	302.27	0.000
Square	3	40.48	13.49	42 943.14	0.0000	0.412	0.1374	0.42	0.746
$q \times q$	1	0.0000	0.000	1.55	< 0.0001	0.094	0.0944	0.29	0.613
$V_{IN} \times V_{IN}$	1	40.01	40.01	127 333.38	0.268	0.225	0.2255	0.69	0.443
$T_{In} \times T_{In}$	1	0.0000	0.0000	0.09	0.000	0.073	0.0733	0.23	0.655
Two-way interaction	3	0.0000	0.0000	1.73	0.778	24.920	8.3067	25.53	0.002
$q \times V_{IN}$	1	0.0000	0.0000	3.90	0.275	0.448	0.4480	1.38	0.294
$V_{IN} \times T_{In}$	1	0.0000	0.0000	0.1	0.105	13.037	13.0368	40.06	0.001
$T_{In} \times q$	1	0.0000	0.0000	1.21	0.769	11.435	11.4354	35.14	0.002
Error	5	0.0000	0.0000	—	0.321	1.627	0.3254	—	—
Lack of fit	3	0.0000	0.0000	—	—	1.627	0.5424	—	—
Pure error	2	0.0000	0.0000	—	—	0.0000	0.0000	—	—
Total	14	2191.74	—	—	—	135.208	—	—	—

TABLE 8 | Regression analysis of the responses.

S. no.	Statics measurement variables	Outlet temperature	Maximum cell temperature	Pressure	Cooling efficiency
1	R^2	99.05%	99.56%	99.89%	98.80%
2	Adjusted R^2	99.34%	98.77%	99.47%	96.63%
3	Predicted R^2	84.78%	92.77%	99.18%	80.75%
4	S	1.45057	1.89647	0.0177221	0.57046

for charging the cells is 3600 s. If the trapped heat inside the cell is not removed during charging, the cells will quickly be damaged. Initially, the generated heat is absorbed by the PCM material; the PCM material absorbs the sensible heat since it is under the solidus temperature. At the time of the melting of PCM, the temperature of the cell remains within the solidus and liquidus temperatures. Moreover, crossing the liquidus temperature, the PCM material is completely melted, and further heating of the cell will increase the temperature at a higher rate.

Figure 9 clearly shows that at 6000 s, the maximum temperature of the cells is 314.372 K, which is well below the allowable temperature limit of the cell. The PCM material controls the maximum temperature due to its large latent heat. Although in solid and liquid phases, it absorbs the sensible heat only. In the solid phase of the PCM, the temperature of the PCM increases by 13.694°C, and in the phase change process, a 3.9°C temperature rise occurs. Figure 9 also shows that the middle six cells are at maximum temperature and the outer cells are at the minimum temperature. This happens due to the lower thermal properties of the PCM material.

5.2 | Mass Fraction Contour of Paraffin Wax at Various Time Intervals in 1 C Charging

Figure 10 shows the mass fraction of the PCM material at different charging times. The melting of the PCM material started at 4800 s. The maximum volume fraction of the PCM at 5000 s is 0.164 at the surface of the middle cells. Further, it will reach 0.991 at 16 000 s or 4.44 h. The PCM material completely melted at the time of 16 400 s. Figures 9 and 10 show that at 1 C charging, the battery temperature is well within the desirable limit and creates no thermal issues within the battery pack.

5.3 | Temperature of the Battery Pack at Paraffin Fin Wax, n-Eicosane, and Copper Foam PCM Material Cooling

Figure 11 demonstrated the consequence of the PCM material on the temperature variation of the battery pack at 5000 s of charging. It is clearly noted from Figure 11 that the extreme temperature of the cell is obtained to be 313.949, 309.901, and 309.63 K in the paraffin wax, n-eicosane, and copper foam. It is important to note that the minimum temperature obtained in the copper foam, even though the cells have better temperature distribution than the paraffin wax and n-eicosane, is due to the higher thermal conductivity of the copper foam.

5.4 | Liquid Fraction of the Battery Pack at Paraffin Fin Wax, n-Eicosane, and Copper Foam PCM Material Cooling

Figure 12 depicts the liquid fraction variation in the paraffin wax, n-eicosane and the copper foam at the charging time of 5000 s in 1 C charging. The liquid fraction in paraffin wax, n-eicosane, and copper foam was obtained to be 0.056, 0.796, and 0.218, respectively. The higher melting efficiency shows the minimum battery pack temperature. it is also noted from Figure 12 that the melting occurs from the surface of the cell and moves toward the outer cell boundaries since the outer surface of the battery pack is considered as the heat sink.

6 | Maximum Cell Temperature at Various Charging Rate

Figure 13 gives the maximum cell temperature at different charging rates in air, paraffin wax, n-eicosane, and copper foam. Figure 13a shows the maximum temperature up to 16 000 s at 1 C charging rates; it is noted that up to 5000 s air, paraffin wax, n-eicosane, and copper foam all have temperatures less than 320 K. At 16 000 s, the air gives a quite high maximum temperature as compared to the PCM material. The maximum temperature of air, paraffin wax, n-eicosane, and copper foam is 336.17, 317.85, 312.78, and 310.86 K respectively. The figure also demonstrated that the performance of the n-eicosane and copper is nearly the same up to 6000 s. Figure 13b describes the comparison of the maximum temperature among air, paraffin wax, n-eicosane, and copper foam at charging rates of 2 C. It is noted from the figure that the copper foam gives the best performance for controlling the maximum temperature among all air and PCM materials. The air maximum temperature is 349.8 K as compared to copper foam temperature 320.1 K, which shows that air cooling is not feasible if the charging rate increases from 2 C.

Figure 13c compares the results of maximum temperature at 3 C charging rates. In 3 C charging, the charging time is reduced to three times the of the 1 C charging. The battery will charge in 1200 s. Figure 13c displays the maximum cell temperature up to 3000 s; the figure depicts that in 1500 s, the maximum temperature of paraffin wax, n-eicosane, and copper is 319.25, 317.14, and 314.45 K, respectively.

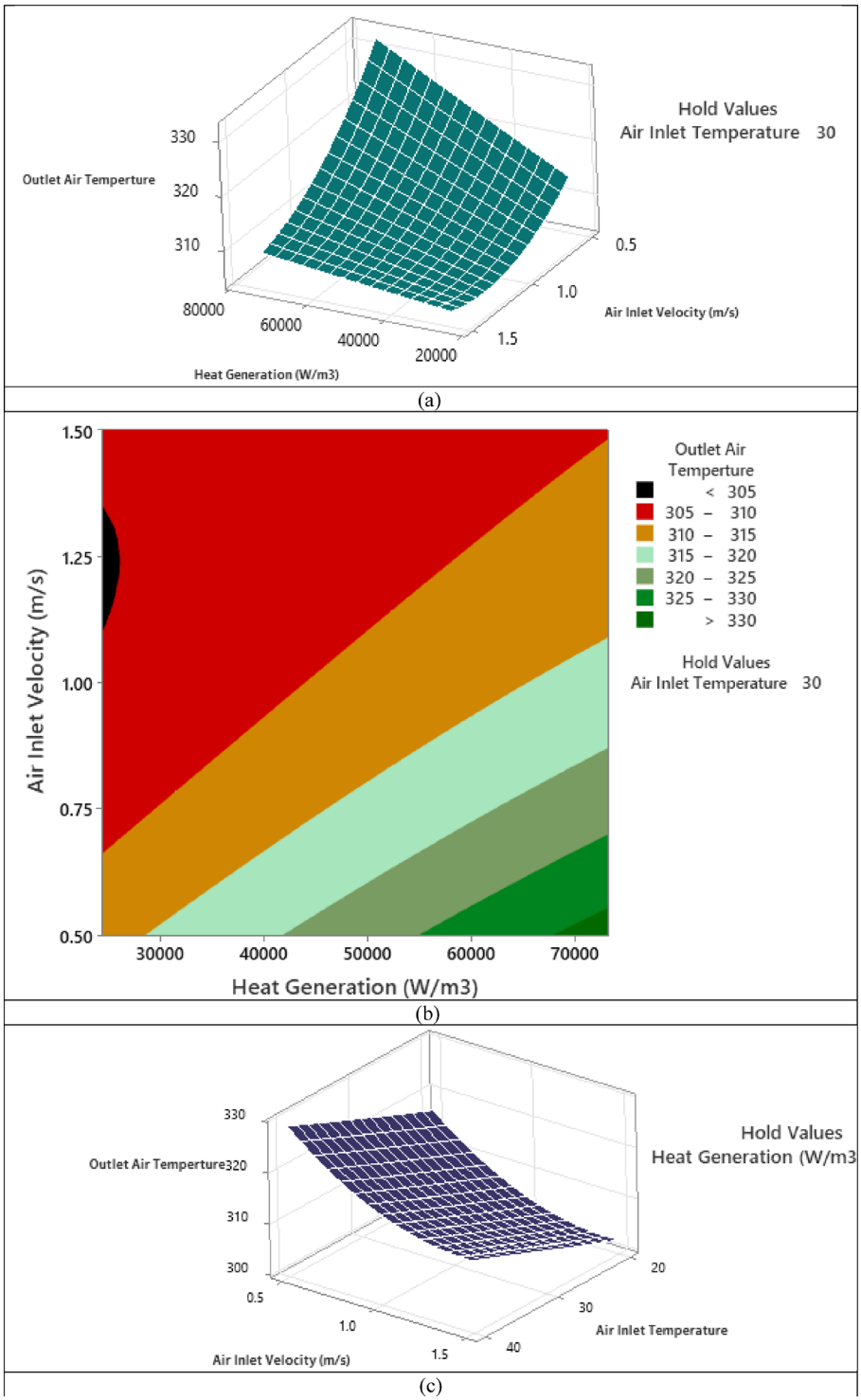

FIGURE 14 | Outlet air temperature variation with input variables. (a) Outlet air temperature variation. (b) 2D plot of the outlet air temperature. (c) Outlet air temperature with air inlet velocity and temperature. (d) Contour plot of the outlet air temperature.

7 | Optimization Results

The response surface methodology (RSM) is an optimization technique used in this research to find the optimal values of inputs. The Box–Behnken Design (BBD) methodology is adopted to define the correlations among the input and response parameters. This design requires the three levels (maximum, middle, minimum) of every input factor for defining the total number of simulation runs. Table 4 represents coded forms of the three levels of the input variables on which responses are dependent. Table 5 represents the total number of runs. Based on the simulation runs, the correlations among the input and response parameters have been determined. The desirability of the responses will define the accuracy of the quadratic models. Table 6 and Table 7 represent the degree of freedom (DF), adjusted sum of square (AdjSS), adjusted mean sum of square (AdjMS), *F*-values, and *p*-values of the responses. Additionally, R^2, R^2(adj), and R^2(pre) values are calculated by following correlations.

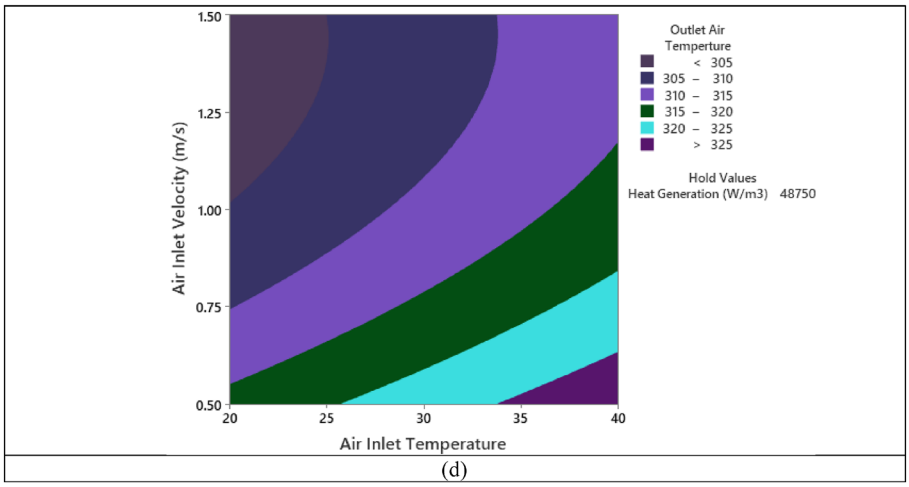

FIGURE 14 | (Continued)

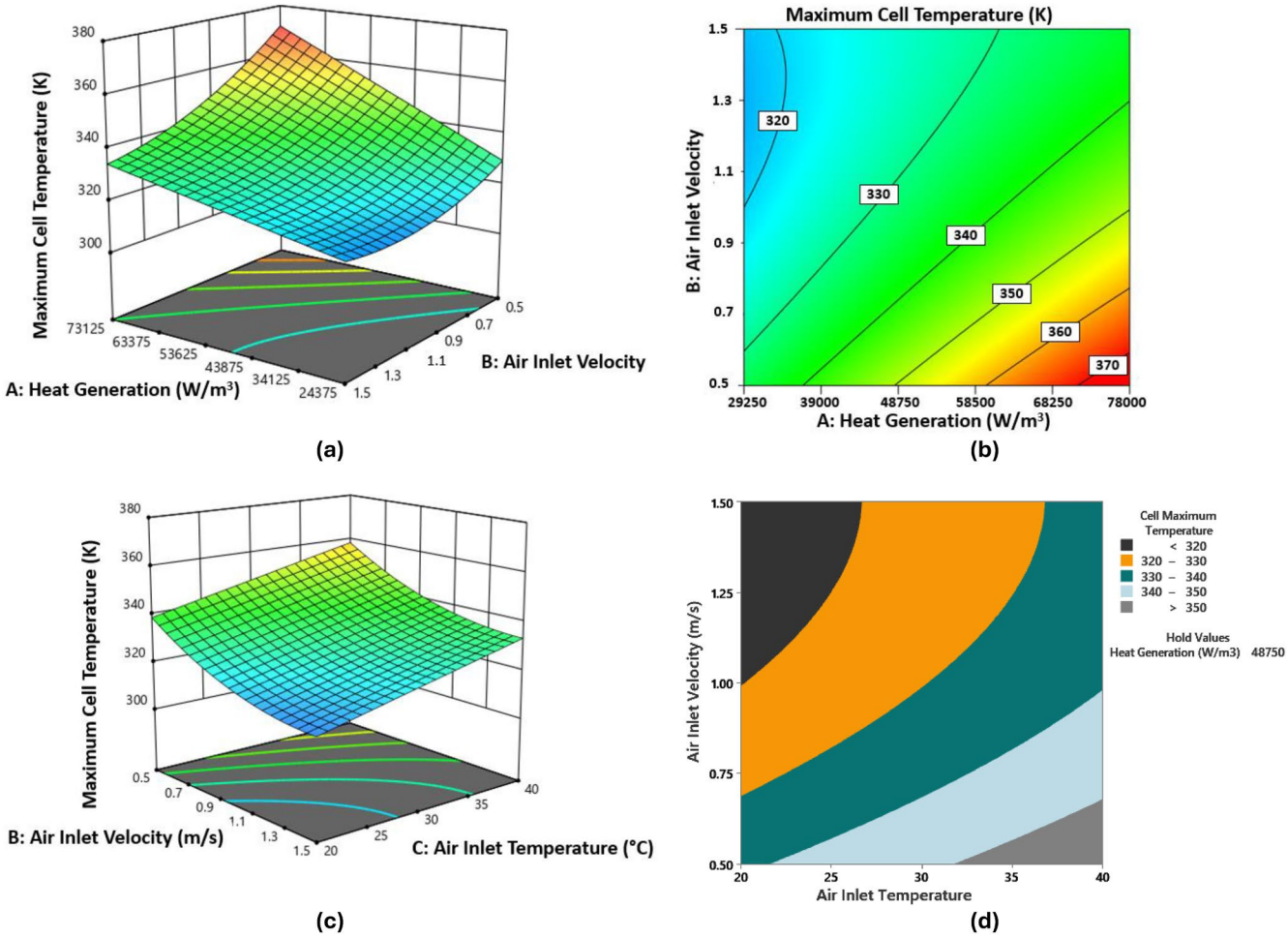

FIGURE 15 | Maximum cell temperature with input variables. (a) Maximum cell temperature surface plot. (b) Contour plot of the maximum cell temperature. (c) 3D surface plot of the cell temperature. (d) Contour plot of maximum cell temperature.

$$R^2 = \frac{\text{Sum of regression squares}}{\text{Sum of suares total}}$$

$$R^2 = \frac{RSS}{SST}$$

$$R^2 = \left(\sum_1^n \left(Y_i^1 - Y\right)\right) / \left(\sum_1^n \left(Y_i - Y\right)\right)$$

$$R^2(\text{Adj}) = 1 - \left(\frac{\left(1 - R^2\right)(N-1)}{(N-p-1)}\right)$$

$$R^2(\text{Pred}) = 1 - \left(\frac{(1 - R^2_{Pred})(N-1)}{(N-p-1)} \right)$$

where N and p are the sample size and the number of independent variables. The R^2 values are essential for the ANOVA analysis. The R^2 value determines how well the data is best fitted with the generated second-order equations of the responses. The following quadratic equations of responses have been generated by the numerical data in terms of the input factors.

$$T_{aO} = 297 + 0.000541q - 31.62V_{\text{in}} + 0.693T_{\text{in}} + 16.52V_{in}^2 + 0.00089T_{\text{in}}^2 - 0.000301qV_{\text{in}} - 0.000001qT_{\text{In}} - 0.052V_{\text{in}}T_{\text{in}}$$

$$T_{C\,\max} = 294.8 + 0.001116q - 49V_{\text{in}} + 1.001T_{\text{in}} + 24.30V_{\text{in}}^2 - 0.00037T_{\text{in}}^2 - 0.000509qV_{\text{in}} + 0.010V_{\text{in}}T_{\text{in}}$$

$$\Delta P = -0.067 + 0.000003q + 6.4722V_{\text{in}} - 0.00027T_{\text{In}} + 13.1680V_{\text{in}}^2 - 0.000028T_{\text{in}}^2 - 0.000001qV_{\text{in}} + 0.00195V_{\text{in}}T_{\text{in}}$$

$$\eta_{\text{Cooling}} = 21.32 - 0.000204q + 4.18V_{\text{in}} - 0.458T_{\text{in}} + 0.99V_{\text{in}}^2 + 0.00141V_{\text{in}}T_{\text{in}} + 0.000027qV_{\text{in}} + 0.000007qT_{\text{in}} - 0.3382V_{\text{in}}T_{\text{in}}$$

How well these equations are fitted with the numerical data is represented in Table 8 by the R^2, R^2 (adj), and R^2(Pre) values. Table 8 shows, the values of R^2 for the outlet air temperature, maximum cell temperature, pressure drop, and cooling efficiency are 99.05%, 99.56%, 99.89%, and 99.80%. it is clearly indicated from the R^2 values that the model is best fitted with numerical data since the values of R^2 are greater than 70%. The adjusted and predicted values of the R^2 are also greater than 70% signifies the best fit of the data with the model equations. The S represents the standard deviation of the residual, the S values are very small which also shows that the model equation is best fitted with the numerical data.

7.1 | Graphical Representations of the Air Outlet Temperature With Input Factors

It is indicated in Figure 14a that as the inlet air velocity rises, the outlet air temperature is reduced due to the increased flow rate of air, which increased air velocity carries more heat that will lower down the cell surface temperature. Figure 14a also indicates that as the heat generation within the cell material increases, the outlet air temperature also increases due to more heat accumulation inside the battery pack. Figure 14b depicts the contour plot of the outlet temperature of air; the green parts of the contour represent the outlet air temperature of more than 330 K, which is represented by the high heat generation and lower flow velocity. Figure 14c depicts the variation of the outlet air temperature with the inlet air velocity and inlet air temperature. It is indicated from Figure 14c that an increase in inlet air temperature enhances the outlet air temperature because the inlet air is already

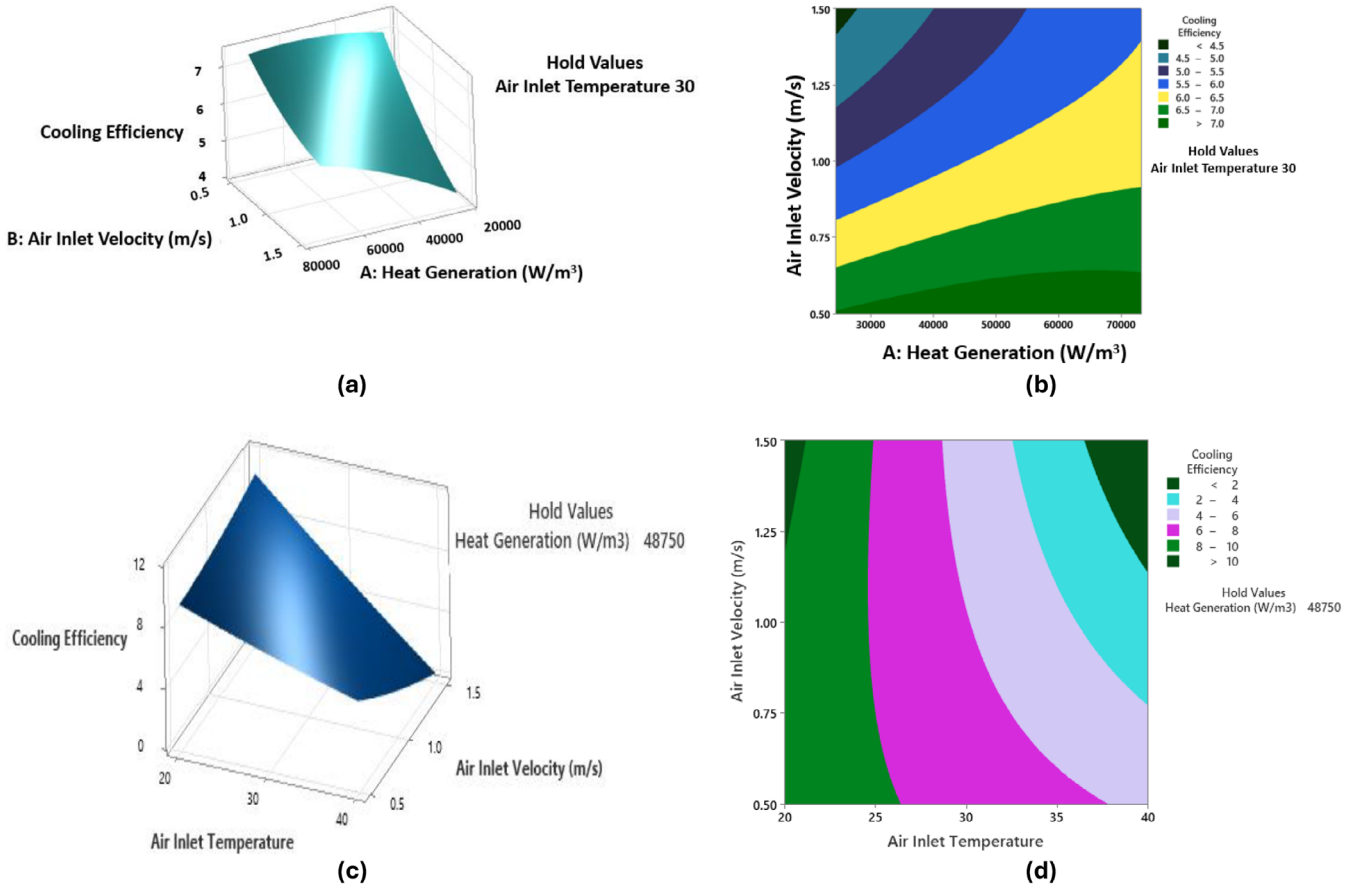

FIGURE 16 | Cooling efficiency variation with the input variables. (a) Cooling efficiency surface plot. (b) Contour plot of the cooling efficiency. (c) Cooling efficiency with air inlet velocity and air inlet temperature. (d) 2D plot of cooling efficiency.

at a higher temperature. On the other hand, the rise in inlet air velocity reduces the outlet air temperature due to more sensible heat carried by the increased mass flow rate of air. The purple color of Figure 14d represents the maximum outlet air temperature of more than 325 K; this region is represented by the higher inlet air temperature and lower inlet air velocity.

7.2 | Maximum Cell Temperature Variation

Figure 15a shows the variation of cell temperature with the heat generation and inlet air velocity. The maximum cell temperature quickly drops due to a rise in air inlet velocity since increasing air velocity enhances the mass flow rate. It also shows that if the heat generation within the cell rises, then the maximum cell temperature also increases since enhanced heat generation increases the input heat supply to the cell material, which increases the internal energy of the cell material. Figure 15b represents the contour plot of the maximum cell temperature with the heat generation and inlet air velocity. The green region of the contour plot shows the maximum cell temperature, which is represented by the maximum heat generation and lower inlet air velocity.

Figure 15c,d shows that as air inlet temperature increases, the maximum cell temperature increases, but an increase in inlet air velocity reduces the maximum cell temperature. The increase in inlet air velocity increases the mass flow rate, which enhances the flow of heat from the battery to the air, resulting in lower cell temperature.

7.3 | Cooling Efficiency Variation With the Input Variables

Cooling efficiency is the ratio of the heat carried out by the air and the heat generated inside the battery pack. Figure 16a depicts that as the heat generation inside the cylinder increases, the cooling efficiency increases since the heat carried out by the air is increased, which enhances the cooling efficiency. Figure 16a also depicts that as air inlet velocity increases, the cooling efficiency reduces due to a higher velocity; contact time is reduced, and a lower amount of heat is carried out by the air. Figure 16b shows the contour plot of the maximum cell temperature; the green part of the contour plot shows a cooling efficiency of more than 7% at higher heat generation and lower inlet air velocity. Figure 16c shows that if the inlet air temperature increases, then the cooling efficiency reduces due to a lower temperature drop at the outlet end of the battery pack. Figure 16d represents the cooling efficiency with the inlet air temperature and inlet air velocity. The green region of the contour plot shows the maximum cooling efficiency of more than 10% at lower inlet temperature and lower inlet velocity.

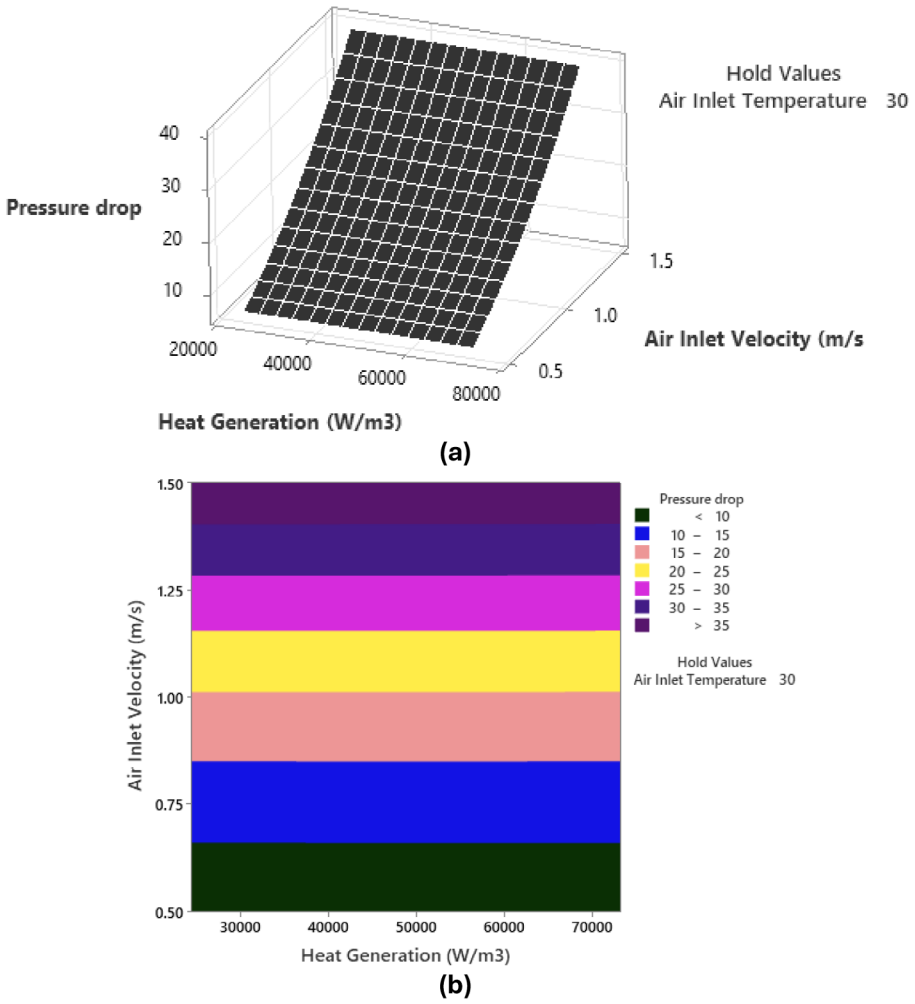

FIGURE 17 | Pressure variation with the input variables. (a) Pressure drop due to air flow around cells surfaces. (b) 2D plot of the pressure drop.

7.4 | Variation of Pressure With Input Parameters

Figure 17a demonstrates that as the inlet air velocity increases, the pressure drop over the battery surface increases due to an increase in form and skin frictional drag on the battery surface. Figure 17b horizontal lines on the contour plot show that the effect of heat generation is neglected on the pressure, but the enhancement of the inlet air velocity increases the pressure drop. The pressure drop in fluid flow mainly occurs due to the loss of kinetic energy in the flow path.

7.5 | Optimization Plot

Figure 18 represents the values of the input and response variables at the optimum conditions with the composite desirability. How well input variables are best fitted with the responses is defined by the desirability. The composite desirability is the geometric mean of the desirability of the individual variables. The numerical value of the desirability varies in the range of 0 to 1. The composite desirability of the optimizing process is 0.6914, showing that the responses' optimum values are best fitted with the corresponding values of the input variables. The optimum values of the input factors obtained by optimization are 42 102 W/m^3, 0.5 m/s inlet air velocity, and 20°C inlet air temperature. Corresponding to these input variables, the maximum cooling efficiency is 9.7276%, the minimum pressure is 6.5281 Pa, and the outlet air temperature is 313.9157 K.

8 | Validation of Results

The current study validated the experimental work of Upadhyay et al. [37] on the 28 cells of the LIB pack. It is observed from Figure 19 that the current study maintained the maximum temperature of the cell lower than the composite phase change material cooling presented experimentally in [37]. The current study lowers the maximum temperature of the cells by around 5 K with the Upadhaya et al. The current investigation used copper foam in place of composite phase change material used by Upadhyay et al. The copper foam performs better in controlling temperature than the composite phase change material due to the higher thermal conductivity of the copper material. The maximum temperature at 50 min of charging in the present study is found to be 66°C as compared to 71°C in Upadhyay et al.

9 | Conclusion

In the current scenario, the Indian government is very much focusing on electric vehicles due to their non-polluting nature and lower running cost than petrol and diesel-operated vehicles. The fast charging of EVs generates high temperatures, which can damage the battery pack and sometimes may cause a fire in the car. To address this issue, this research article investigated the effect of air, paraffin wax, n-eicosane, and copper foam cooling

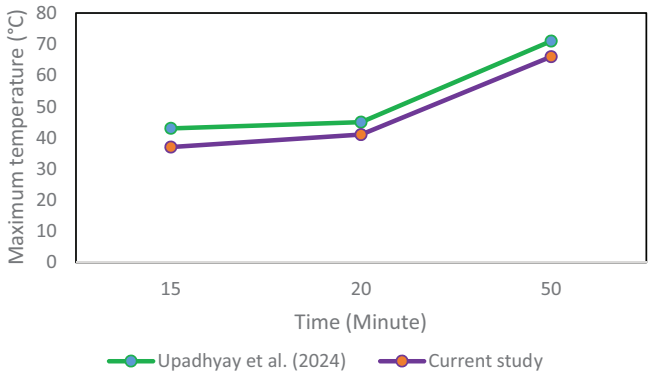

FIGURE 19 | Validation of maximum battery pack temperature with Upadhyay et al. [37].

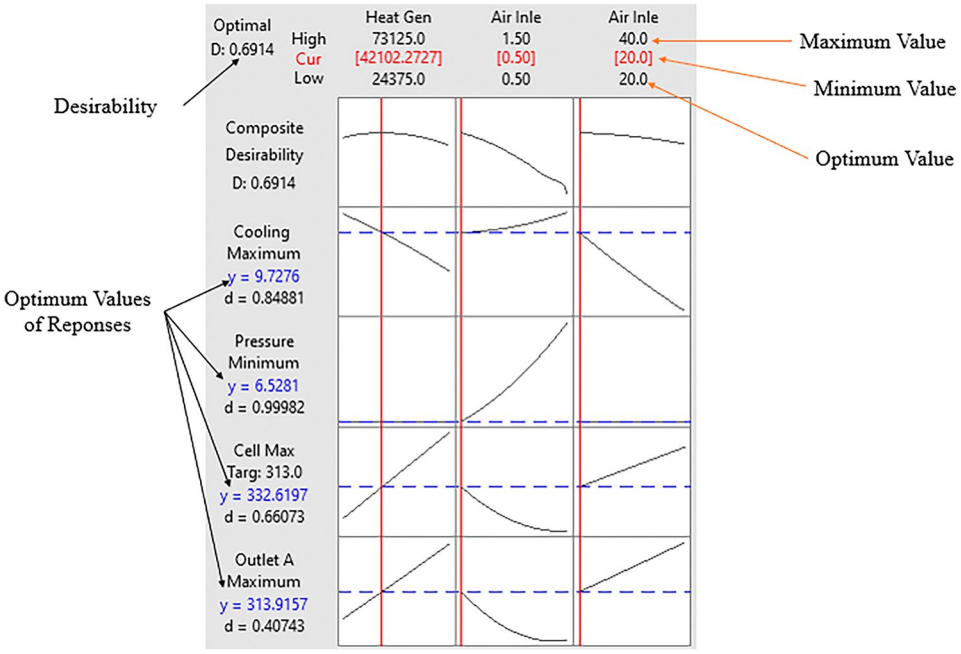

FIGURE 18 | Response optimization plot.

on the 28-cell battery pack. ANSYS Fluent 18.1 was used to simulate the problem, and the results were displayed in the form of temperature, velocity, and pressure contour. The RSM was used to optimize the system to determine the inlet air temperature, inlet air velocity, and the effect of heat generation on the battery pack temperature. The following outcomes were obtained from this study.

1. The air could be used for the cooling of the battery pack up to the 1 and 2 C charging. The higher charging rates, namely 3, 4, and 5 C, air cooling cannot control the battery pack temperature in a feasible range.
2. The optimum conditions for the air cooling are heat generation 42 102 W/m^3, air inlet velocity 0.5 m/s, and inlet air temperature 20°C beyond the heat generation 42 102 W/m^3, the enhanced heat generation increases the cell temperature very high level.
3. The higher heat generation, PCM material control, maintains the temperature for a long period due to latent heat storage. For 1 C charging, the paraffin wax, n-eicosane, and copper foam temperatures at 4.44 h of charging are 317.42, 312.78, and 31.86 K, as compared to air cooling 336.7 K.
4. At 2 C charging rates, the maximum temperature of the battery pack in paraffin wax, n-eicosane, copper foam and air are 343, 339.5, 320.1, and 349.8 K respectively.
5. The copper foam performed best at the 3 C charging; at 3 C charging, the maximum cell temperature in 50 min of charging gives 339 K as compared to 345 and 341.21 K in paraffin wax and n-eicosane.
6. The validation study shows that the copper foam gives better performance than the composite phase change material. At 50 min, charging the copper foam and CPCM gives the 66°C and 71°C maximum cell temperature, respectively.
7. The copper foam gives a lower temperature and maintains the uniformity in the maximum cell temperature as compared to other PCM materials. The PCM materials fail to cool all the cells uniformly due to the lower thermal conductivity of the PCM materials.

10 | Recent Advances in Electrode Material and Physics-Based Modeling

The anode and cathode are the important parts of a LIB, which work to store and release lithium ions during charging and discharging. The chemical composition of the electrodes affects the cell's performance during charging and discharging. The recent advances in the electrode material are based on the enhanced energy density, fire safety, and economy. The currently used anode and cathode materials are graphite and the LCO (lithium cobalt oxide), LMO (lithium manganese oxide), NMC (nickel manganese cobalt oxide), and NCA (lithium nickel cobalt aluminum oxide) slurry pasted on the copper and aluminum foil. The recent research is mainly focused on removing the cobalt from the cathode material and making it rich in nickel composition. These cobalt, nickel, and magnesium represent the 51% recycling cost of the battery. The silicon and metal alloy are used in place of graphite in the anode due to their high capacity and volume change at the time of working. The carbon porous electrode is currently preferred due to higher thermal conductivity and can manage the side reactions. Currently, the lithium metal has been explored to use as the anode material due to higher energy density, but due to safety issues, the current research is under investigation. The physics-based modeling considers the electrode is made by the porous material filled with electrolyte. It uses the physical and chemical principles in the internal structure of the cell, which is based on the conservation of mass and charge, including the studies of ion transport and electrochemical reactions. The Doyle Full Newman (DFN) modeling is very widely used in cell design, predicting battery aging and advanced control. The advanced control includes the estimation of the state of charge (SoC) and state of health (SoH) for the battery.

Funding

The authors have nothing to report.

Conflicts of Interest

The authors declare no conflicts of interest.

Data Availability Statement

The data that support the findings of this study are available on request from the corresponding author. The data are not publicly available due to privacy or ethical restrictions.

References

1. J. Wen, D. Zhao, and C. Zhang, "An Overview of Electricity Powered Vehicles: Lithium-Ion Battery Energy Storage Density and Energy Conversion Efficiency," *Renewable Energy* 162 (2020): 1629–1648, https://doi.org/10.1016/j.renene.2020.09.055.

2. Y. Li, K. Li, Y. Xie, J. Liu, C. Fu, and B. Liu, "Optimized Charging of Lithium-Ion Battery for Electric Vehicles: Adaptive Multistage Constant Current–Constant Voltage Charging Strategy," *Renewable Energy* 146 (2020): 2688–2699, https://doi.org/10.1016/j.renene.2019.08.077.

3. F. Yi, E. Jiaqiang, B. Zhang, et al., "Effects Analysis on Heat Dissipation Characteristics of Lithium-Ion Battery Thermal Management System Under the Synergism of Phase Change Material and Liquid Cooling Method," *Renewable Energy* 181 (2022): 472–489, https://doi.org/10.1016/j.renene.2021.09.073.

4. P. Ramadass, B. Haran, R. White, and B. N. Popov, "Capacity Fade of Sony 18650 Cells Cycled at Elevated Temperatures: Part II. Capacity Fade Analysis," *Journal of Power Sources* 112 (2022): 614–620, https://doi.org/10.1016/S0378-7753(02)00473-1.

5. S. Arora, "Selection of Thermal Management System for Modular Battery Packs of Electric Vehicles: A Review of Existing and Emerging Technologies," *Journal of Power Sources* 400 (2018): 621–640, https://doi.org/10.1016/j.jpowsour.2018.08.020.

6. P. Qin, J. Sun, X. Yang, and Q. Wang, "Battery Thermal Management System Based on the Forced-Air Convection: A Review," *eTransportation* 7 (2021): 1–22, https://doi.org/10.1016/j.etran.2020.100097.

7. A. Sharma, Y. Patil, R. Krishnaiah, B. Ashok, A. Garg, and L. Gao, "Study on Effect of Diverse Air Inlet Arrangement on Thermal Management of Cylindrical Lithium-Ion Cells," *Heat Transfer* 49 (2020): 4626–4656, https://doi.org/10.1002/htj.21845.

8. M. Al-Zareer, I. Dincer, and M. A. Rosen, "A Thermal Performance Management System for Lithium-Ion Battery Packs," *Applied Thermal*

Engineering 165 (2019): 1–17, https://doi.org/10.1016/j.applthermaleng.2019.114378.

9. S. D. V. S. S. V. Siruvuri and P. R. Budarapu, "Studies on Thermal Management of Lithium-Ion Battery Pack Using Water as the Cooling Fluid," *Journal of Energy Storage* 29 (2020): 1–14, https://doi.org/10.1016/j.est.2020.101377.

10. M. Akbarzadeh, T. Kalogiannis, L. Jin, D. Karimi, J. Van Mierlo, and M. Berecibar, "Experimental and Numerical Thermal Analysis of a Lithium-Ion Battery Module Based on a Novel Liquid Cooling Plate Embedded With Phase Change Material," *Journal of Energy Storage* 50 (2022): 1–17, https://doi.org/10.1016/j.est.2022.104673.

11. Kausthubharam, P. K. Koorata, S. Panchal, R. Fraser, and M. Fowler, "Investigation of the Thermal Performance of Biomimetic Minichannel-Based Liquid-Cooled Large Format Pouch Battery Pack," *Journal of Energy Storage* 84 (2024): 1–12, https://doi.org/10.1016/j.est.2024.110928.

12. Z. Jiang, H. Li, Z. Sun, and Z. Qu, "Experimental Study on 18650 Lithium-Ion Battery-Pack Cooling System Composed of Heat Pipe and Reciprocating Air Flow With Water Mist," *International Journal of Heat and Mass Transfer* 222 (2023): 1–12, https://doi.org/10.1016/j.ijheatmasstransfer.2024.125171.

13. J. Chen, S. Kang, E. Jiaqiang, et al., "Effects of Different Phase Change Material Thermal Management Strategies on the Cooling Performance of the Power Lithium Ion Batteries: A Review," *Journal of Power Sources* 442 (2019): 1–18, https://doi.org/10.1016/j.jpowsour.2019.227228.

14. D. Lu, N. Cui, J. Zhou, and C. Li, "Hybrid Cooling System With Phase Change Material and Liquid Microchannels to Prevent Thermal Runaway Propagation Within Lithium-Ion Battery Packs," *Applied Thermal Engineering* 247 (2024): 1–16, https://doi.org/10.1016/j.applthermaleng.2024.123118.

15. Z. An, X. Chen, L. Zhao, and Z. Gao, "Numerical Investigation on Integrated Thermal Management for a Lithium- Ion Battery Module With a Composite Phase Change Material and Liquid Cooling," *Applied Thermal Engineering* 163 (2019): 1–10, https://doi.org/10.1016/j.applthermaleng.2019.114345.

16. Q. Xin, T. Yang, H. Zhang, J. Yang, J. Zeng, and J. Xiao, "Experimental and Numerical Study of Lithium-Ion Battery Thermal Management System Using Composite Phase Change Material and Liquid Cooling," *Journal of Energy Storage* 71 (2023): 1–16, https://doi.org/10.1016/j.est.2023.108003.

17. A. Rahmani, M. Dibaj, and M. Akrami, "Design and Simulation of Battery Thermal Management Systems for Electric Vehicles Using MATLAB Simulink," *Journal of Energy Storage* 111 (2025): 1–18, https://doi.org/10.1016/j.est.2025.115398.

18. H. A. Hasan, H. Togun, A. M. Abed, H. I. Mohammed, and T. Armaghani, "Cooling Lithium-Ion Batteries With Silicon Dioxide-Water Nanofluid: CFD Analysis," *Renewable and Sustainable Energy Reviews* 208 (2025): 1–15, https://doi.org/10.1016/j.rser.2024.115007.

19. W. Li, A. Li, A. C. Yin Yuen, et al., "Optimisation of PCM Passive Cooling Efficiency on Lithium-Ion Batteries Based on Coupled CFD and ANN Techniques," *Applied Thermal Engineering* 259 (2025): 1–17, https://doi.org/10.1016/j.applthermaleng.2024.124874.

20. A. Joshi, R. Banerjee, and K. Nidhul, "Thermo-Hydraulic Performance and Entropy Generation Analysis of Lithium-Ion Battery With Porous Medium for Temperature Homogeneity," *International Journal of Ambient Energy* 46, no. 1 (2025): 1–15, https://doi.org/10.1080/01430750.2024.2447551.

21. T. F. Yang, P. Y. Lin, C. Y. Lin, W. M. Yan, and S. Rashidi, "Study on Thermal Aspects of Lithium-Ion Battery Packs With Phase Change Material and Air Cooling System," *Case Studies in Thermal Engineering* 53 (2024): 1–16, https://doi.org/10.1016/j.csite.2023.103809.

22. S. Xin, C. Wang, and H. Xi, "Thermal Management Scheme and Optimization of Cylindrical Lithium-Ion Battery Pack Based on Air Cooling and Liquid Cooling," *Applied Thermal Engineering* 224 (2023): 1–12, https://doi.org/10.1016/j.applthermaleng.2023.120100.

23. A. Chakir, I. El, G. Anas, E. Maâkoul, S. Saadeddine, and M. Meziane, "Comprehensive Study of Serpentine Heat Exchangers in Thermoelectric Coolers: Experimental and Numerical Approaches," 61 (2025): 1–14, https://doi.org/10.1007/s00231-024-03529-1.

24. M. Tousi and M. Najafi, "Innovative Hybrid Nano/Dielectric Fluid Cooling System for the New Cylindrical Shaped Li-Ion Batteries," *International Journal of Thermal Sciences* 195 (2024): 1–14, https://doi.org/10.1016/j.ijthermalsci.2023.108634.

25. F. Dilbaz, F. Selimefendigil, and H. F. Öztop, "Comparisons of Different Cooling Systems for Thermal Management of Lithium-Ion Battery Packs: Phase Change Material, Nano-Enhanced Channel Cooling and Hybrid Method," *Journal of Energy Storage* 90 (2024): 1–20, https://doi.org/10.1016/j.est.2024.111865.

26. A. Thiru Kumaran and S. Hemavathi, "Optimization of Lithium-Ion Battery Thermal Performance Using Dielectric Fluid Immersion Cooling Technique," *Process Safety and Environmental Protection* 189 (2024): 768–781, https://doi.org/10.1016/j.psep.2024.06.117.

27. W. Cheng, M. Chen, D. Ouyang, J. Weng, L. Zhao, and Y. Chen, "Investigation of the Thermal Performance and Heat Transfer Characteristics of the Lithium-Ion Battery Module Based on an Oil-Immersed Cooling Structure," *Journal of Energy Storage* 79 (2024): 1–11, https://doi.org/10.1016/j.est.2023.110184.

28. Y. Gao, F. Liu, J. Wang, W. R. Ye, and X. Meng, "Influence of the Copper Foam Shape on Thermal Performance of Phase-Change Material," *Journal of Energy Storage* 36 (2021): 1–9, https://doi.org/10.1016/j.est.2021.102416.

29. K. Boomsma and D. Poulikakos, "On the Effective Thermal Conductivity of a Three-Dimensionally Structured ¯Uid-Saturated Metal Foam," *International Journal of Heat and Mass Transfer* 44 (2001): 827–836, https://doi.org/10.1016/S0017-9310(00)00123-X.

30. H. Najafi Khaboshan, F. Jaliliantabar, A. Adam Abdullah, and S. Panchal, "Improving the Cooling Performance of Cylindrical Lithium-Ion Battery Using Three Passive Methods in a Battery Thermal Management System," *Applied Thermal Engineering* 227 (2023): 1–12, https://doi.org/10.1016/j.applthermaleng.2023.120320.

31. M. M. Heyhat, S. Mousavi, and M. Siavashi, "Battery Thermal Management With Thermal Energy Storage Composites of PCM, Metal Foam, Fin and Nanoparticle," *Journal of Energy Storage* 28 (2020): 1–14, https://doi.org/10.1016/j.est.2020.101235.

32. H. Xiao, J. Wang, Z. Liu, and W. Liu, "Turbulent Heat Transfer Optimization for Solar Air Heater With Variation Method Based on Exergy Destruction Minimization Principle," *International Journal of Heat and Mass Transfer* 136 (2019): 1096–1105, https://doi.org/10.1016/J.IJHEATMASSTRANSFER.2019.03.071.

33. A. S. Yadav and J. L. Bhagoria, "A CFD (Computational Fluid Dynamics) Based Heat Transfer and Fluid Flow Analysis of a Solar Air Heater Provided With Circular Transverse Wire Rib Roughness on the Absorber Plate," *Energy* 55 (2023): 1127–1142, https://doi.org/10.1016/J.ENERGY.2013.03.066.

34. A. Uniyal and Y. K. Prajapati, "Impact of Fin Arrangement on Heat Transfer and Melting Characteristics of Phase Change Material," *Journal of Thermal Science* 33 (2024): 435–456, https://doi.org/10.1007/s11630-024-1925-0.

35. C. Ji, Z. Qin, Z. Low, S. Dubey, F. H. Choo, and F. Duan, "Non-Uniform Heat Transfer Suppression to Enhance PCM Melting by Angled Fins," *Applied Thermal Engineering* 129 (2018): 269–279, https://doi.org/10.1016/j.applthermaleng.2017.10.030.

36. F. Zhang, F. Lu, B. Liang, et al., "Thermal Performance Analysis of a New Type of Branch-Fin Enhanced Battery Thermal Management PCM Module," *Renewable Energy* 206 (2023): 1049–1063, https://doi.org/10.1016/j.renene.2023.02.083.

37. D. Upadhyay, V. Mujadia, R. Daruwala, A. Lakdawala, and D. Shah, "Investigation on Performance of Composite Phase Change Material Based Thermal Management of Electrical Battery," *International Journal on Interactive Design and Manufacturing* 18 (2024): 4285–4294, https://doi.org/10.1007/s12008-024-01994-w.